



A tensor model for the calibration of air-coupled ultrasonic sensor arrays in 3D imaging

Raphael Müller^{*,1}, Gianni Allevato², Matthias Rutsch³, Christoph Haugwitz, Tianyi Liu (刘添翼), Mario Kupnik, Marius Pesavento⁴

Department of Electrical Engineering and Information Technology, TU Darmstadt, Merckstr. 25, 64283 Darmstadt, Germany

ARTICLE INFO

Keywords:

Airborne ultrasound
Array response modeling
Dictionary learning
Low-rank tensor approximation
MIMO imaging
Sparse representation

ABSTRACT

Arrays of ultrasonic sensors are capable of 3D imaging in air and an affordable supplement to other sensing modalities, such as radar, lidar, and camera, i.e. in heterogeneous sensing systems. However, manufacturing tolerances of air-coupled ultrasonic sensors may lead to amplitude and phase deviations. Together with artifacts from imperfect knowledge of the array geometry, there are numerous factors that can impair the imaging performance of an array. We propose a reference-based calibration method to overcome possible limitations. First, we introduce a novel tensor signal model to capture the characteristics of piezoelectric ultrasonic transducers (PUTs) and the underlying multidimensional nature of a multiple-input multiple-output (MIMO) sensor array. Second, we formulate and solve an optimization problem based on this model to obtain the calibrated parameters of the array. Third, we assess both our model and the commonly used analytic model using real data from a 3D imaging experiment. The experiment reveals that our array response model we learned with calibration data yields an imaging performance similar to that of the analytic array model, which requires perfect array geometry information.

1. Introduction

When considering imaging with ultrasound (US), the first thing that comes to mind is medical imaging [1–3]. With the advent of cost-efficient high-power sensors, however, three-dimensional (3D) ultrasonic imaging, which combines two-dimensional (2D) direction finding and range estimation, has been extended to operate in air [4]. In general, air-coupled ultrasonic imaging builds on phased array technology and uses similar image formation principles as medical sonography and MIMO radar, e.g. beamforming techniques [5] and synthetic apertures [6].

The main advantages of US over other air-coupled sensing modalities are its low deployment cost, its robustness against particles in the air, e.g. smoke, dust, or rainfall, as well as its ability to operate independently of the lighting conditions [7,8]. In addition, acoustic waves offer distinct imaging characteristics compared to electromagnetic (EM) waves or light due to the different system parameters such as the wave propagation speed or material reflectivity. This makes air-coupled US attractive for heterogeneous sensing systems where different sensing

modalities can complement each other as frequently encountered in autonomous driving [9] or, more recently, in healthcare [10].

The major obstacle in air-coupled US is the poor coupling of acoustic waves into air, as well as the high attenuation and the low propagation speed of US in air as compared to fluids or tissue [11–14]. In contrast to medical sonography, the requirement for large coverage areas of airborne US, along with the reduced speed of sound in air lead to large propagation delays, thereby slowing down the image frame rate. Additionally, the larger wavelengths of US systems in air lead to a reduced angular resolution compared to medical US if arrays of the same aperture size are considered. Thus, air-coupled US faces a variety of challenges that distinguish it from medical US. The latter is also comparatively mature whereas research on 3D imaging with an US array in air has only recently become a study subject as well [15].

Air-coupled ultrasonic sensors, also referred to as transducers, are realized with different materials and principles, resulting in varying degrees of sensitivity, mechanical robustness, and costs [16]. The inherent properties of the materials used and the production tolerances of low cost transducers lead to variations in the directivity pattern and

* Corresponding author.

E-mail address: raphael.mueller@nt.tu-darmstadt.de (R. Müller).

¹ Student Member, EURASIP.

² Present address: Hottinger Brüel & Kjær GmbH, Im Tiefen See 45, 64293, Darmstadt, Germany.

³ Present address: Robert Bosch GmbH, Daimlerstr. 6, 71229, Leonberg, Germany.

⁴ Member, EURASIP.

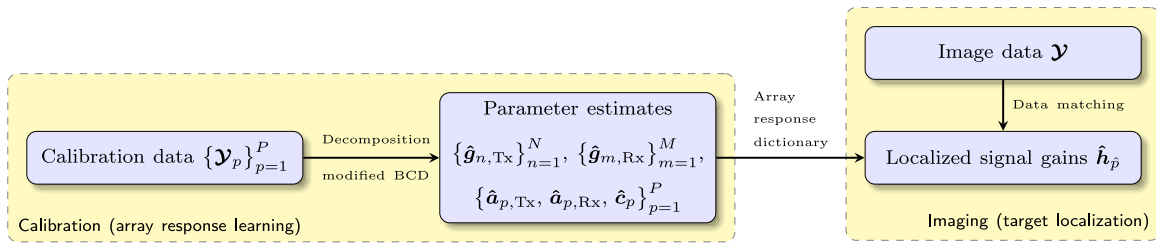


Fig. 1. Flowchart for the proposed calibration and imaging steps: calibration data $\{\mathcal{Y}_p\}_{p=1}^P$ from P distinct reference positions, characterized by 3D coordinates, is measured to estimate the parameters $\{\hat{g}_{n,\text{Tx}}\}_{n=1}^N$, $\{\hat{g}_{m,\text{Rx}}\}_{m=1}^M$, and $\{\hat{a}_{p,\text{Tx}}, \hat{a}_{p,\text{Rx}}, \hat{c}_p\}_{p=1}^P$. With those, targets in an unknown scene are localized from image data \mathcal{Y} by selecting target position estimates \hat{p} from the P candidate positions of the array response dictionary learned during calibration. Finally, the target signal gain $\hat{h}_{\hat{p}}$ of each target detected is estimated.

frequency responses. Furthermore, differing resonance frequencies in the transmit and receive mode, respectively, result in nonreciprocal transceiver characteristics of PUTs such that no common array manifold for transmission and reception exists. These and other factors, e.g. aging or exposure of an imaging system to environmental conditions such as temperature fluctuations, urge the need to learn the transducer array responses from training data, particularly within complex heterogeneous sensing systems where describing the array response analytically is often impractical.

In this work, we consider a bistatic MIMO imaging system with a uniform rectangular array (URA) of PUT elements as a prototype US system for 3D imaging in air. PUTs are a popular choice for this as they deliver a high output pressure at their resonance frequency while being available for a low unit price, making them attractive for large array configurations in various applications [17–20]. Concomitant disadvantages include a comparatively small relative bandwidth as well as fluctuations in the element directivity and phase response [21]. As PUTs are often too large to be placed at half-wavelength ($\lambda/2$) spacing, the array is embedded into a waveguide for grating-lobe-free beamforming [22]. While the waveguide offers protection in harsh environments and enables flexible array shape designs, it introduces further uncertainties in the array response and increases the overall complexity of the imaging system. Therefore, it is necessary to investigate whether these uncertainties adversely affect the imaging performance when using the commonly employed analytic point source model, and to explore how anomalous array responses can be accurately modeled.

We propose a novel multidimensional array model to capture artifacts and uncertainties from imperfections in both the individual transducer elements as well as the array configuration. The model parameters are learned from reference-based calibration data. High-resolution 3D imaging is accomplished with the virtual array concept where the aperture is spanned by the Kronecker product of the receive array and multiple, spatially displaced transmit sensors. Each transmitter emits US pulses into a sparse scenery such that at the receive array, target echoes are recorded in the image data tensor \mathcal{Y} . During image formation, indexed positions \hat{p} of each potential target are estimated from \mathcal{Y} based on the spatial signatures corresponding to P candidate positions that have been learned previously at the calibration stage. For each source position \hat{p} , a corresponding gain $\hat{h}_{\hat{p}}$ is estimated, whose magnitude is displayed in the final image (Fig. 1).

1.1. State of the art and own contributions

Array calibration addresses the problem of modeling errors in the array response, most commonly due to unknown sensor amplitudes and phases, mutual coupling (electrical, mechanical, and acoustic cross-talk) between the array elements, or inaccurate knowledge of their relative positions [23]. Remedies for these imperfections differ based on the availability of additional calibration measurements. Non-reference-based, or *autocalibration*, methods do not require calibration targets at known locations and perform calibration and target localization either alternately or jointly on the same data using parametric models,

e.g., the sensor locations, the complex gains, or the coupling matrix are jointly estimated during the image formation [24–27]. Calibration is achieved by exploiting the specific geometry of the array [28–30], especially in the case of partly calibrated arrays [31–33] and higher-order statistics of the associated measurements [34], or other concepts such as low-rank modeling or sparsity [35–37]. However, the parametric approach of joint calibration and imaging requires a structured model with only few degrees of freedom. In the context of air-coupled US, Ramamohan et al. recently investigated joint calibration and one-dimensional (1D) direction-of-arrival (DOA) estimation with a linear array assuming a highly structured array manifold [38].

Contrary to autocalibration, reference-based calibration methods are more flexible in terms of error modeling and suggest superior imaging performance of a stationary system after calibration [39–41]. Other recent studies such as [42–44] reveal that the majority of calibration methods in the literature, both reference-based and non-reference-based, consider linear measurement models, even though the underlying imaging principles are of a multilinear nature, comprising a multidimensional data tensor with a transmitter, receiver, frequency, and time dimension, respectively. In such a case, using multilinear algebra for dictionary learning of the multidimensional data is more appropriate [45]. Recently, Guo et al. demonstrated such a multilinear approach to the calibration of a bistatic MIMO radar where a rank-one CPD model was considered for each source [46]. Similar approaches were later pursued by Sun et al. [47] and Chen et al. [48]. In our previous work [49], we applied low-rank tensor factorization to calibration data and exploited sparsity in the image formation [50]. That approach with a generic tensor model is designed for arrays composed of identical transceiver elements with identical transmit and receive magnitude responses.

In this work, we take the particular manufacturing tolerances and transceiver characteristics of PUTs into account and propose a novel tensor signal model that captures the multidimensional structure of an air-coupled ultrasonic sensor array for MIMO imaging. We learn the parameters of our proposed tensor signal model jointly from measurements of the entire volume-of-interest (VOI), i.e. the angular field-of-view (FOV) in a given range interval. In a testbed deployed in our anechoic chamber at TU Darmstadt, we additionally assess the performance of our proposed method with a phased array for 3D imaging where the PUTs are combined with a 3D-printed waveguide. In summary, the key contributions of this article are:

- (1) We introduce a novel tensor signal model that accounts for varying element transceiver characteristics in air-coupled ultrasonic MIMO sensor arrays with nonuniform transmitter and receiver magnitude responses and nonuniform element patterns. This makes our model also of interest for other array processing applications, including sonar and radar.
- (2) We learn the array response from reference-based calibration measurements using targets at known locations. An optimization problem is formulated to jointly estimate all tensor model parameters.

- (3) We apply a unique parameterization to the proposed tensor model and derive a modified block coordinate descent (BCD) method that exhibits highly parallel, closed-form solutions of the corresponding subproblems in each set of block variables. We prove that the modified BCD method converges to a stationary point of the calibration problem.
- (4) We test the proposed calibration method using synthetic data and real measurements recorded with prototype hardware. A 3D imaging example serves as a proof of concept for the usability of the dictionary of array responses learned from calibration measurements.
- (5) We compare the imaging quality of our proposed tensor model after calibration with the conventional analytic point source model, which in the case of our testbed data reveals to be a valid model.

1.2. Notation and outline

We use the italic letter x , the boldface lowercase italic letter \mathbf{x} , the boldface uppercase italic letter \mathbf{X} , and the boldface uppercase calligraphic italic letter \mathcal{X} to denote a scalar, a vector, a matrix, and a general multi-way array, respectively. The (i_1, i_2, \dots) th scalar element of \mathcal{X} is denoted by $[\mathcal{X}]_{i_1, i_2, \dots}$ and a colon instead of a fixed index indicates the selection of all entries of the corresponding mode. Subtensors with all but one index fixed (fibers) are assumed to be column vectors and subtensors with all but two indices fixed (slices) are treated as matrices. Unfolding the tensor \mathcal{X} to its mode w is denoted by $\text{unf}_w(\mathcal{X})$ and yields matrix $\mathbf{X}_{(w)}$. The all-one vector of length I is denoted by $\mathbf{1}_I$ and $\text{vec}(\cdot)$ returns its multidimensional argument reshaped into a vector, while $\text{Diag}(\cdot)$ returns a square matrix with the elements of the vector argument on the main diagonal and zero everywhere else, respectively. Symbols \odot , \otimes , \circledast and \circ denote Hadamard multiplication, Kronecker multiplication, column-wise Kronecker (Khatri-Rao) multiplication, and outer tensor multiplication, respectively. The complex conjugate, transpose, and Hermitian transpose are represented by $(\cdot)^*$, $(\cdot)^T$, and $(\cdot)^H$, respectively, while $(\cdot)^{(i)}$ denotes the i th iterate of a variable. Taking the Euclidean norm or the Frobenius norm is indicated by $\|\cdot\|_2$ and $\|\cdot\|_F$, respectively. Finally, $\arg(\cdot)$ returns the principal angle of its complex argument while operators $\text{Re}(\cdot)$ and $\text{Im}(\cdot)$ return the real and imaginary part of their argument, respectively.

The rest of this article is organized as follows: Section 2 introduces the tensor signal model that is used to formulate the estimation problem for calibration in Section 3, where it is solved with a modified BCD method. The resulting parameter estimates are then used for imaging in Section 4. Results from simulations as well as experiments with real data are presented in Section 5 and concluding remarks with future research directions are given in Section 6.

2. Signal model for calibration

Consider a single and static point target at a position indexed by integer p in the far field of a co-located MIMO transceiver array. In polar coordinates, the position of this target can be, e.g., characterized by $(r_p, \vartheta_p, \varphi_p)$, where r_p , ϑ_p , and φ_p represent the target range, azimuth angle and elevation angle, respectively. The target is repeatedly exposed to US pulses emitted from one of the transceiver elements. In total, N different transmitters are used for excitation and, w.l.o.g., we index the reference sensor with $n = 1$. Under the narrowband assumption, the spatial displacement of a transmitter element w.r.t. the reference sensor yields a corresponding phase shift in the waveform at the point target. At position p , the phase shifts of all N transmitter elements relative to the reference sensor are characterized by the transmit steering vector $\mathbf{a}_{p, \text{Tx}} \in \mathbb{C}^N$ [51]. Furthermore, the complex gain $[\mathbf{a}_{p, \text{Tx}}]_n$ also captures the propagation delay and the path attenuation experienced by the n th transmitter as a result from additional transceiver structures, such as an attached waveguide [52].

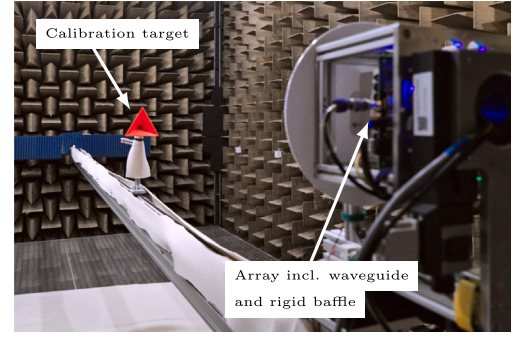


Fig. 2. Measurement setup in an anechoic chamber to obtain data for the calibration technique proposed in Section 3.

According to the Huygens-Fresnel principle, the wave impinging on a target initiates a reflecting wave that travels back to the transceiver array. Hence in the receiver path, the far field point target is viewed as a point source transmitting an echo signal to the array. For an arbitrary array geometry, the M -element array response to the echo signal originating from a target at position p is described by a general receive steering vector $\mathbf{a}_{p, \text{Rx}} \in \mathbb{C}^M$ [53]. Similar to $\mathbf{a}_{p, \text{Tx}}$, each receive steering vector consists of receiver-dependent complex gains based on individual characteristics, e.g. point responses, propagation delays, and path attenuations.

For the calibration of the measurement system, a reflector is set up at distinct but known positions $p = 1, \dots, P$ in an anechoic chamber (Fig. 2). Compared to its surrounding, the reflector provides a strong echo that approximates a point source in free field. Sequentially, each transmitter $n = 1, \dots, N$ fires a series of T acoustic pulses, also referred to as bursts [54]. Each burst emerges from the physical operating principle of a PUT, i.e. after applying multiple periods of a sinusoidal electrical signal with constant excitation frequency to the active transducer.

After reflection at the target object, the incoming echo pulse is measured at the receive array and converted back from the acoustic to the electrical domain based on the receiver characteristics of the respective PUT elements. Thus, the data acquisition principle is similar as in MIMO radar or medical US. However, passband signals in air-coupled US can be directly sampled without downconversion due to the comparably low carrier frequency of $f_0 = 40$ kHz. After analog-to-digital conversion of the sampled echo signal per transmitter and burst, a rectangular window of length $N_{\text{rect}} = 2^{12}$ is applied to each of the M receive sequences to filter out undesired reflections from near field clutter or ghost targets from multipath propagation. In the following, we consider measurements in the frequency domain by applying the discrete Fourier transform (DFT) to the received time signals.

The PUTs regarded in this work have a narrow relative bandwidth of about 3%, i.e., most of the signal energy is spread across the frequency range from 39.4 kHz to 40.6 kHz. Based on the sampling frequency $f_s = 195$ kHz of the measurement system, we select $L = 24$ frequency bins equally spaced by $N_{\text{rect}}^{-1} f_s \approx 48$ Hz that contain the significant signal power around the average receive resonance frequency. The measurements of each transmitter $n = 1, \dots, N$ are then arranged in a three-way array of dimension $M \times L \times T$, similar to the data tensor used in MIMO radar [55]. As in radar, air-coupled US imaging also uses the short time measurements for range estimation. In the following, we introduce a novel tensor signal model that accounts for nonidentical magnitude responses of distinct transceiver elements in a sensor array.

In the frequency band of interest, we model the transmit and receive characteristics (transfer functions) of the n th transmitter and the m th receiver on the L dominant DFT bins by the real-valued frequency response vectors $\mathbf{g}_{n, \text{Tx}}$ and $\mathbf{g}_{m, \text{Rx}}$. The US transceivers can be operated in transmit or receive mode with a fast switch between both modes. We

remark, however, that due to manufacturing tolerances, the frequency responses of different sensors are generally different and also the transmit and receive responses within the same sensor generally differ due to the distinct resonance frequencies for both operating modes [56].

The propagation time of a burst affects the phase of the DFT of the receive pulse proportionally to the range of the target at position p . For a point target, the phase increment over frequency is generally linear, however, for generality we allow arbitrary phase increments in the phase response $c_p \in \mathbb{C}^L$, which is modeled with a unit modulus property, i.e. $|[c_p]_\ell| = 1$, $\ell = 1, \dots, L$. We combine $\mathbf{g}_{n,\text{Tx}}$, $\mathbf{g}_{m,\text{Rx}}$, and c_p into the frequency vector

$$\mathbf{b}_{n,m,p} = \mathbf{g}_{n,\text{Tx}} \odot \mathbf{g}_{m,\text{Rx}} \odot c_p \quad (1)$$

of the pulse from the n th transmitter to the m th receiver after reflection from the target at position p , which models the input–output relationship of the transceivers as a linear time-invariant (LTI) system.

Lastly, the modulation of each pulse sequence, the path attenuation between the reference sensors of the transmit and receive array, and the reflectivity of the point target at position p are all modeled by the signal gain vector $\mathbf{h}_p \in \mathbb{C}^T$. Thus $[\mathbf{h}_p]_r$, i.e. the r th entry of the gain vector \mathbf{h}_p , does not only describe particular system attributes such as the amplitude and the phase of the r th transmit pulse but also the acoustic cross-section of the scatterer.

We assume, w.l.o.g., that the signal gain vector does not change between different transmit pulses for the same target, i.e. $\mathbf{h}_p = [\mathbf{h}_p]_1 \mathbf{1}_T$. In our approach, however, we admit arbitrary, possibly nonidentical entries in \mathbf{h}_p to model artifacts of the data acquisition system such as sample offsets that occur during reception as well as variations in the pulse amplitudes. For simplicity, we assume that all transmitters use the same pulse waveform (envelope) so that \mathbf{h}_p is independent of the transmitter index n .

Using all of the parameters introduced above, we model each pulse that travels from transmitter n to receiver m as the trilinear term in (1) weighted by scalars $[a_{p,\text{Tx}}]_n \in \mathbb{C}$ and $[a_{p,\text{Rx}}]_m \in \mathbb{C}$. Evidently, this expression is also dependent on the target position indexed by p . A pulse sequence over T distinct time instants, referred to as snapshots, over the L frequency bins of interest then yields the $L \times T$ rank-1 matrix

$$[a_{p,\text{Tx}}]_n [a_{p,\text{Rx}}]_m (\mathbf{g}_{n,\text{Tx}} \odot \mathbf{g}_{m,\text{Rx}} \odot c_p) \mathbf{h}_p^T. \quad (2)$$

Furthermore, the collection of all receive measurements initiated by all transmitters yields a four-way array $\mathcal{Y}_p \in \mathbb{C}^{N \times M \times L \times T}$ for every calibration target position $p = 1, \dots, P$. We model the p th tensor as

$$\mathcal{Y}_p = \sum_{n=1}^N \sum_{m=1}^M (e_n \odot a_{p,\text{Tx}}) \circ (e_m \odot a_{p,\text{Rx}}) \circ (\mathbf{g}_{n,\text{Tx}} \odot \mathbf{g}_{m,\text{Rx}} \odot c_p) \circ \mathbf{h}_p + \mathcal{Z}_p, \quad (3)$$

where e_i is the standard basis vector of compatible dimension with entries $[e_i]_j = 1$ for $i = j$ and $[e_i]_j = 0$ for $i \neq j$, and $\mathcal{Z}_p \in \mathbb{C}^{N \times M \times L \times T}$ represents additive measurement noise. The basis vectors impose a masking on all but one entry in $a_{p,\text{Tx}}$ and $a_{p,\text{Rx}}$, respectively, such that (3) is composed of the slices in (2).

2.1. Relation to other tensor models

According to (3), the receive measurements $\{\mathcal{Y}_p\}_{p=1}^P$ from P target positions are coupled by the magnitude responses $\{\mathbf{g}_{n,\text{Tx}}\}_{n=1}^N$ and $\{\mathbf{g}_{m,\text{Rx}}\}_{m=1}^M$. A special case arises if all transceivers have identical transmit and receive magnitude responses, i.e. $\mathbf{g}_{n,\text{Tx}} = \mathbf{g}_{n',\text{Tx}}$ and $\mathbf{g}_{m,\text{Rx}} = \mathbf{g}_{m',\text{Rx}}$ for $n, n' = 1, \dots, N$ and $m, m' = 1, \dots, M$, respectively. In this instance, we may introduce a common transmit magnitude response \mathbf{g}_{Tx} for all n and a common receive magnitude response \mathbf{g}_{Rx} for all m , respectively, such that the model in (3) reduces to

$$\tilde{\mathcal{Y}}_p = a_{p,\text{Tx}} \circ a_{p,\text{Rx}} \circ (\mathbf{g}_{\text{Tx}} \odot \mathbf{g}_{\text{Rx}} \odot c_p) \circ \mathbf{h}_p + \mathcal{Z}_p. \quad (4)$$

For a single position p , the noise-free part of (4) admits a rank-1 CPD, which roots in the canonical decomposition (CANDECOMP) [57] and

the parallel factor (PARAFAC) model [58]. Measurement tensors of different target positions, however, still share a common transmit and magnitude response under (4), which is not addressed by the general positionwise rank-1 CPD approximation

$$\mathcal{Y}_p \approx a_{p,\text{Tx}} \circ a_{p,\text{Rx}} \circ b_p \circ \mathbf{h}_p. \quad (5)$$

Unlike our proposed tensor model, the rank-1 CPD approximation (5) is in this case associated with a model mismatch. For studies on the multi-rank CPD of a measurement tensor, where each rank-1 component corresponds to the signal from one of multiple targets, we refer the reader to [50].

Another interesting link to multilinear algebra is given by the block-term decomposition of a third-order tensor [59]. If we rearrange our P fourth-order tensors $\{\mathcal{Y}_p\}_{p=1}^P$ from (3) into the coupled third-order tensors

$$\mathcal{Y}_{\text{virt},p} = \left[[\mathcal{Y}_p]_{1,\dots,1}, \dots, [\mathcal{Y}_p]_{N,\dots,N} \right]^T \in \mathbb{C}^{NM \times L \times T} \quad (6)$$

for $p = 1, \dots, P$ with a virtual array spanned by NM transceiver elements, we can factorize the measurements into

$$\mathcal{Y}_{\text{virt},p} = \left(\mathbf{A}_p \mathbf{B}_p^T \right) \circ \mathbf{h}_p \quad (7)$$

for $p = 1, \dots, P$ using the diagonal matrix

$$\mathbf{A}_p = \text{Diag}(a_{p,\text{Tx}} \otimes a_{p,\text{Rx}}) \in \mathbb{C}^{NM \times NM} \quad (8)$$

for $p = 1, \dots, P$, which is formed from the virtual array steering vector corresponding to the target at position p , and the frequency matrix

$$\mathbf{B}_p = \left(c_p^T \otimes \mathbf{G}_{\text{Tx}}^T \otimes \mathbf{G}_{\text{Rx}}^T \right)^T \in \mathbb{C}^{L \times NM} \quad (9)$$

for $p = 1, \dots, P$ with

$$\mathbf{G}_{\text{Tx}} = [\mathbf{g}_{1,\text{Tx}}, \dots, \mathbf{g}_{N,\text{Tx}}] \in \mathbb{C}^{L \times N} \quad (10)$$

and

$$\mathbf{G}_{\text{Rx}} = [\mathbf{g}_{1,\text{Rx}}, \dots, \mathbf{g}_{M,\text{Rx}}] \in \mathbb{C}^{L \times M}. \quad (11)$$

The factorization in (7) is similar to the rank- $(I, I, 1)$ block-term decomposition of (6) given by $\mathcal{Y}_{\text{virt},p} = \sum_{r=1}^R (\tilde{\mathbf{A}}_{p,r} \tilde{\mathbf{B}}_{p,r}^T) \circ \tilde{\mathbf{h}}_{p,r}$ with $\tilde{\mathbf{A}}_{p,r} \in \mathbb{C}^{NM \times I}$ and $\tilde{\mathbf{B}}_{p,r} \in \mathbb{C}^{L \times I}$ for $I \leq \min(L, NM)$, and tensor rank R [60]. In contrast to matrices $\tilde{\mathbf{A}}_{p,r}$ and $\tilde{\mathbf{B}}_{p,r}$, which do not exhibit any specific structure, our matrices \mathbf{A}_p and \mathbf{B}_p are structured according to (8) and (9), respectively. Furthermore, our frequency matrix \mathbf{B}_p is not guaranteed to have full column rank, e.g. if $L < NM$, but allows a more descriptive insight on the physical behavior of the imaging system. Thus, we prefer (7) over the “regular” rank- $(I, I, 1)$ decomposition of the tensor in (6) for the considered application. As a final remark, we note that all third-order tensors $\{\mathcal{Y}_{\text{virt},p}\}_{p=1}^P$ are coupled by the magnitude response matrices \mathbf{G}_{Tx} and \mathbf{G}_{Rx} in (10) and (11), respectively, which is not captured by the positionwise rank- $(I, I, 1)$ decomposition and highlights the novelty of our proposed signal model in (3).

2.2. Unfolding of the tensor signal model

When dealing with the tensor model in (3), it is often convenient to operate with the corresponding matrix unfoldings instead. Unfolding, also known as matricization, rearranges any W -way array $\mathcal{X} \in \mathbb{C}^{I_1 \times \dots \times I_W}$ into matrices $\mathbf{X}_{(w)} \in \mathbb{C}^{I_w \times I_1 \dots I_{w-1} I_{w+1} \dots I_W}$ for modes $w = 1, \dots, W$. An intuitive way to matricize a tensor is to cyclically permute its modes. The unfoldings of a four-way array $\mathcal{X} \in \mathbb{C}^{I_1 \times I_2 \times I_3 \times I_4}$ are given by

$$\begin{aligned} \text{unf}_1(\mathcal{X}) &= \mathbf{X}_{(1)} \\ &:= [\mathcal{X}]_{:,1,1}, [\mathcal{X}]_{:,2,1}, \dots, [\mathcal{X}]_{:,J_3,1}, \dots, [\mathcal{X}]_{:,J_3,J_4}, \end{aligned} \quad (12a)$$

$$\begin{aligned} \text{unf}_2(\mathcal{X}) &= \mathbf{X}_{(2)} \\ &:= [\mathcal{X}]_{1,1,\dots,1}, [\mathcal{X}]_{1,1,\dots,2}, \dots, [\mathcal{X}]_{1,1,\dots,J_4}, \dots, [\mathcal{X}]_{J_1,1,\dots,J_4}, \end{aligned} \quad (12b)$$

$$\text{unf}_3(\mathcal{X}) = \mathbf{X}_{(3)} \\ := [([\mathcal{X}]_{1,1,1,:\dots}, [\mathcal{X}]_{2,1,1,:\dots}, \dots, [\mathcal{X}]_{I_1,1,1,:\dots}, \dots, [\mathcal{X}]_{I_1, I_2, 1,:\dots}], \quad (12c)$$

$$\text{unf}_4(\mathcal{X}) = \mathbf{X}_{(4)} \\ := [([\mathcal{X}]_{:,1,1,:\dots})^\top, ([\mathcal{X}]_{:,2,1,:\dots})^\top, \dots, ([\mathcal{X}]_{:, I_2, 1,:\dots})^\top, \dots, ([\mathcal{X}]_{:, I_2, I_3,:\dots})^\top]^\top. \quad (12d)$$

Let us further define the factor matrices

$$\mathbf{A}_{p,\text{Tx}} = \text{Diag}(\mathbf{a}_{p,\text{Tx}}) \otimes \mathbf{1}_M^\top \in \mathbb{C}^{N \times NM}, \quad (13a)$$

$$\mathbf{A}_{p,\text{Rx}} = \mathbf{1}_N^\top \otimes \text{Diag}(\mathbf{a}_{p,\text{Rx}}) \in \mathbb{C}^{M \times NM}, \quad (13b)$$

$$\mathbf{H}_p = \mathbf{h}_p \mathbf{1}_{NM}^\top \in \mathbb{C}^{T \times NM}. \quad (13c)$$

Using the matricization in [61] and the permutation scheme in [62], the following properties w.r.t. our tensor model in (3) hold for $\mathcal{Z}_p = \mathbf{0}$, i.e. the noiseless case:

$$\text{unf}_1(\mathcal{Y}_p) = \mathbf{Y}_{p(1)} = \mathbf{A}_{p,\text{Tx}} (\mathbf{H}_p \otimes \mathbf{B}_p \otimes \mathbf{A}_{p,\text{Rx}})^\top \in \mathbb{C}^{N \times MLT}, \quad (14a)$$

$$\text{unf}_2(\mathcal{Y}_p) = \mathbf{Y}_{p(2)} = \mathbf{A}_{p,\text{Rx}} (\mathbf{A}_{p,\text{Tx}} \otimes \mathbf{H}_p \otimes \mathbf{B}_p)^\top \in \mathbb{C}^{M \times NLT}, \quad (14b)$$

$$\text{unf}_3(\mathcal{Y}_p) = \mathbf{Y}_{p(3)} = \mathbf{B}_p (\mathbf{A}_{p,\text{Rx}} \otimes \mathbf{A}_{p,\text{Tx}} \otimes \mathbf{H}_p)^\top \in \mathbb{C}^{L \times NMT}, \quad (14c)$$

$$\text{unf}_4(\mathcal{Y}_p) = \mathbf{Y}_{p(4)} = \mathbf{H}_p (\mathbf{B}_p \otimes \mathbf{A}_{p,\text{Rx}} \otimes \mathbf{A}_{p,\text{Tx}})^\top \in \mathbb{C}^{T \times NML}. \quad (14d)$$

In the following, we estimate the model parameters by applying all four unfoldings on the measurement tensors in a modified BCD procedure that leads to parallel alternating univariate optimization problems [63].

3. Modified block coordinate descent procedure

The signal model in (3) provides us with parameters $\mathbf{g}_{n,\text{Tx}}$, $\mathbf{g}_{m,\text{Rx}}$, $\mathbf{a}_{p,\text{Tx}}$, $\mathbf{a}_{p,\text{Rx}}$, \mathbf{c}_p , and \mathbf{h}_p that characterize the array for a single point target at position p . Ultimately, we aim to describe a given but unknown array for an arbitrary scene composed of multiple targets at different and unknown positions. According to the superposition principle, a scene with multiple targets can be described as the superposition of multiple, independent single-source cases [64]. Thus, we propose a reference-based calibration method where the unknown parameters are estimated from P single-source scenarios with known positions of the calibration target. This provides us with the ability to handle scenarios with multiple unknown targets after calibration.

Using the measurement system in the anechoic chamber, we place a reflector at P different positions and record the respective measurement tensors, each one following (3). The collection of tensors $\{\mathcal{Y}_p\}_{p=1}^P$ is then matched jointly to our model in (3) to determine the parameter estimates $\{\hat{\mathbf{g}}_{n,\text{Tx}}\}_{n=1}^N$, $\{\hat{\mathbf{g}}_{m,\text{Rx}}\}_{m=1}^M$, and $\{\hat{\mathbf{a}}_{p,\text{Tx}}, \hat{\mathbf{a}}_{p,\text{Rx}}, \hat{\mathbf{c}}_p, \hat{\mathbf{h}}_p\}_{p=1}^P$. This parameter estimation process is cast as an optimization problem (see (15a)–(15l) in Box I) with cost function

$$f\left(\{\mathbf{g}_{n,\text{Tx}}\}_{n=1}^N, \{\mathbf{g}_{m,\text{Rx}}\}_{m=1}^M, \{\mathbf{a}_{p,\text{Tx}}, \mathbf{a}_{p,\text{Rx}}, \mathbf{c}_p, \mathbf{h}_p\}_{p=1}^P\right) \\ = \sum_{p=1}^P \left\| \mathcal{Y}_p - \sum_{n=1}^N \sum_{m=1}^M (\mathbf{e}_n \circ \mathbf{a}_{p,\text{Tx}}) \circ (\mathbf{e}_m \circ \mathbf{a}_{p,\text{Rx}}) \circ (\mathbf{g}_{n,\text{Tx}} \circ \mathbf{g}_{m,\text{Rx}} \circ \mathbf{c}_p) \circ \mathbf{h}_p \right\|_F^2, \quad (16)$$

which is designed to match the noise-free array output model corresponding to (3) to all calibration measurements $\{\mathcal{Y}_p\}_{p=1}^P$ in a least-squares (LS) sense.

The constraints in (15b)–(15f) and (15h)–(15l) are introduced to address trivial scaling invariances. Generally, if (15a) is minimized without these constraints, then not only $\{\mathbf{g}_{n,\text{Tx}}^*\}_{n=1}^N$, $\{\mathbf{g}_{m,\text{Rx}}^*\}_{m=1}^M$, and $\{\mathbf{a}_{p,\text{Tx}}^*, \mathbf{a}_{p,\text{Rx}}^*, \mathbf{c}_p^*, \mathbf{h}_p^*\}_{p=1}^P$ are minimizers to (15a), but also $\{\tilde{\mathbf{g}}_{n,\text{Tx}}^*\}_{n=1}^N$, $\{\tilde{\mathbf{g}}_{m,\text{Rx}}^*\}_{m=1}^M$, and $\{\tilde{\mathbf{a}}_{p,\text{Tx}}^*, \tilde{\mathbf{a}}_{p,\text{Rx}}^*, \tilde{\mathbf{c}}_p^*, \tilde{\mathbf{h}}_p^*\}_{p=1}^P$ yield the same objective function value in (15a) for $\tilde{\mathbf{g}}_{n,\text{Tx}}^* = \kappa_{n,\text{gTx}} \mathbf{g}_{n,\text{Tx}}^*$, $\tilde{\mathbf{g}}_{m,\text{Rx}}^* = \kappa_{m,\text{gRx}} \mathbf{g}_{m,\text{Rx}}^*$, $\tilde{\mathbf{a}}_{p,\text{Tx}}^* = \kappa_{p,\text{aTx}} \mathbf{a}_{p,\text{Tx}}^*$, $\tilde{\mathbf{a}}_{p,\text{Rx}}^* = \kappa_{p,\text{aRx}} \mathbf{a}_{p,\text{Rx}}^*$, $\tilde{\mathbf{c}}_p^* = \kappa_{p,c} \mathbf{c}_p^*$, and $\tilde{\mathbf{h}}_p^* = \kappa_{p,h} \mathbf{h}_p^*$, where the coefficients $\kappa_{n,\text{gTx}}$ and $\kappa_{m,\text{gRx}}$ are positive real-valued, $\kappa_{p,\text{aTx}}$ and

$\kappa_{p,\text{aRx}}$ are arbitrary complex, $\kappa_{p,c}$ is unit modulus, i.e. $|\kappa_{p,c}| = 1$, and $\kappa_{p,h} = (\kappa_{n,\text{gTx}} \kappa_{m,\text{gRx}} \kappa_{p,\text{aTx}} \kappa_{p,\text{aRx}} \kappa_{p,c})^{-1}$. Rotations of the global phase are prevented by keeping the first entry of every optimization variable other than \mathbf{h}_p real-valued. Scaling ambiguities are further avoided by employing norm constraints on $\mathbf{a}_{p,\text{Tx}}$ and $\mathbf{a}_{p,\text{Rx}}$, respectively. Constraint (15h) resolves the scaling ambiguity between the transmit and receive frequency response vectors, $\mathbf{g}_{n,\text{Tx}}$ and $\mathbf{g}_{m,\text{Rx}}$, in the objective function (16) by fixing the transmit reference sensor $n = 1$. On the DFT bins that carry relevant signal power, the frequency responses of the n th transmitter and m th receiver, respectively, are furthermore restricted in (15i)–(15l) to take real and strictly positive values in the interval $[\epsilon, 1]$ for some small constant $\epsilon > 0$. Lastly, (15g) follows from the unit modulus property of the phase response vector \mathbf{c}_p .

Problem (15) is jointly nonconvex, with a multivariate objective function (15a). For each individual variable, however, the problem can be reformulated in an equivalent convex subproblem when the remaining variables are fixed. Hence, (15) can be solved by various iterative techniques such as gradient projection and the successive convex approximation framework [65]. We choose the BCD method that approximates the multilinear objective of the optimization problem by a series of approximate problems in which all but one optimization variable are fixed, leading to univariate subproblems [66].

Applying the BCD method straight to problem (15) results in subproblems that are nonconvex due to the constraints. As nonconvex problems are in general difficult to solve, we relax the nonconvex constraints in each of the subproblems and then show that these constraints can always be satisfied by appropriate scaling. This modification of the BCD method convexifies the subproblems such that they exhibit closed-form solutions. Additionally, each approximate problem is separable into further subproblems with independent variables such that the update of any block variable can be done in parallel. This makes our method attractive for implementation on modern parallel hardware architectures such as graphics processing units (GPUs), field-programmable gate arrays (FPGAs), and multicore digital signal processors (DSPs). Further parallelization can be achieved with the successive convex approximation framework in [65].

Each approximate problem only depends on one set of variables, hence, only one factor in the multilinear product. The following subsections introduce the approximate problems for each block variable and the corresponding solutions. We denote the iterates of the different block variables after the update and before the parameter scaling in iteration i of the modified BCD method as $\{\mathbf{g}_{n,\text{Tx}}^{(i+1)}\}_{n=1}^N$, $\{\mathbf{g}_{m,\text{Rx}}^{(i+1)}\}_{m=1}^M$ and $\{\mathbf{a}_{p,\text{Tx}}^{(i+1)}, \mathbf{a}_{p,\text{Rx}}^{(i+1)}, \mathbf{c}_p^{(i+1)}, \mathbf{h}_p^{(i+1)}\}_{p=1}^P$, respectively.⁵ The iterates of the different block variables in the i th iteration of the modified BCD method after the parameter scaling are denoted as

$$\tilde{\mathbf{g}}_{n,\text{Tx}}^{(i+1)} = \kappa_{n,\text{gTx}} \mathbf{g}_{n,\text{Tx}}^{(i+1)}, \quad (17a)$$

$$\tilde{\mathbf{g}}_{m,\text{Rx}}^{(i+1)} = \kappa_{m,\text{gRx}} \mathbf{g}_{m,\text{Rx}}^{(i+1)}, \quad (17b)$$

$$\tilde{\mathbf{a}}_{p,\text{Tx}}^{(i+1)} = \kappa_{p,\text{aTx}} (\kappa_{\text{gTx}} \circ \mathbf{a}_{p,\text{Tx}}^{(i+1)}), \quad (17c)$$

$$\tilde{\mathbf{a}}_{p,\text{Rx}}^{(i+1)} = \kappa_{p,\text{aRx}} (\kappa_{\text{gRx}} \circ \mathbf{a}_{p,\text{Rx}}^{(i+1)}), \quad (17d)$$

$$\tilde{\mathbf{c}}_p^{(i+1)} = \kappa_{p,c} \mathbf{c}_p^{(i+1)}, \quad (17e)$$

$$\tilde{\mathbf{h}}_p^{(i+1)} = \kappa_{p,h} \mathbf{h}_p^{(i+1)}, \quad (17f)$$

for $n = 1, \dots, N$, $m = 1, \dots, M$, and $p = 1, \dots, P$, respectively, where

$$\kappa_{\text{gTx}} = [\kappa_{1,\text{gTx}}, \dots, \kappa_{N,\text{gTx}}] = [1, (\max_{\ell} [\mathbf{g}_{2,\text{Tx}}^{(i+1)}]_{\ell})^{-1}, \dots, (\max_{\ell} [\mathbf{g}_{N,\text{Tx}}^{(i+1)}]_{\ell})^{-1}]^\top \in \mathbb{R}_+^N, \quad \kappa_{\text{gRx}} = [\kappa_{1,\text{gRx}}, \dots, \kappa_{M,\text{gRx}}] = [(\max_{\ell}$$

⁵ We note that the order in which the variables are updated can be modified and does not need to follow the sequence presented here. It is, however, mandatory by the BCD method to always use the latest available values of all parameters when updating one block variable of interest.

$$\begin{aligned}
& \min_{\substack{\{\mathbf{g}_{n,\text{Tx}}\}_{n=1}^N, \\ \{\mathbf{g}_{m,\text{Rx}}\}_{m=1}^M, \\ \{\mathbf{a}_{p,\text{Tx}} \in \mathbb{C}^N, \mathbf{a}_{p,\text{Rx}} \in \mathbb{C}^M, \mathbf{c}_p \in \mathbb{C}^L, \mathbf{h}_p \in \mathbb{C}^T\}_{p=1}^P}} \\
& \text{s.t.} \quad \text{Im}([\mathbf{a}_{p,\text{Tx}}]_1) = 0, \quad p = 1, \dots, P, \tag{15b} \\
& \quad \|\mathbf{a}_{p,\text{Tx}}\|_2^2 - N = 0, \quad p = 1, \dots, P, \tag{15c} \\
& \quad \text{Im}([\mathbf{a}_{p,\text{Rx}}]_1) = 0, \quad p = 1, \dots, P, \tag{15d} \\
& \quad \|\mathbf{a}_{p,\text{Rx}}\|_2^2 - M = 0, \quad p = 1, \dots, P, \tag{15e} \\
& \quad [c_p]_1 - 1 = 0, \quad p = 1, \dots, P, \tag{15f} \\
& \quad |[c_p]_\ell| - 1 = 0, \quad p = 1, \dots, P, \ell = 2, \dots, L, \tag{15g} \\
& \quad \mathbf{g}_{1,\text{Tx}} = \mathbf{1}_L, \tag{15h} \\
& \quad -[\mathbf{g}_{n,\text{Tx}}]_\ell + \varepsilon \leq 0, \quad n = 2, \dots, N, \ell = 1, \dots, L, \tag{15i} \\
& \quad \max_\ell [\mathbf{g}_{n,\text{Tx}}]_\ell - 1 = 0, \quad n = 2, \dots, N, \ell = 1, \dots, L, \tag{15j} \\
& \quad -[\mathbf{g}_{m,\text{Rx}}]_\ell + \varepsilon \leq 0, \quad m = 1, \dots, M, \ell = 1, \dots, L, \tag{15k} \\
& \quad \max_\ell [\mathbf{g}_{m,\text{Rx}}]_\ell - 1 = 0, \quad m = 1, \dots, M, \ell = 1, \dots, L, \tag{15l}
\end{aligned}$$

Box 1.

$[\mathbf{g}_{1,\text{Rx}}^{(i+1)}]_\ell^{-1}, \dots, (\max_\ell [\mathbf{g}_{M,\text{Rx}}^{(i+1)}]_\ell^{-1})^\top \in \mathbb{R}_+^M$, $\kappa_{p,c} = [\mathbf{c}_p^{(i+1)}]_1^*$, $\kappa_{p,h} = (\kappa_{p,\mathbf{a}_{\text{Tx}}} \kappa_{p,\mathbf{a}_{\text{Rx}}} \kappa_{p,c})^{-1}$, while $\kappa_{p,\mathbf{a}_{\text{Tx}}}$ and $\kappa_{p,\mathbf{a}_{\text{Rx}}}$ are chosen such that the first entry in $\mathbf{a}_{p,\text{Tx}}^{(i+1)}$ and $\mathbf{a}_{p,\text{Rx}}^{(i+1)}$ becomes real-valued, respectively, and the respective norm constraints (15c) and (15e) are fulfilled.

3.1. Update of $\{\mathbf{a}_{p,\text{Tx}}\}_{p=1}^P$

We start our modified BCD method by relaxing problem (15) to remove the constraints (15b) and (15c), which can always be satisfied by the proposed rescaling in (17). Following the definitions (13b) and (13c) for the factor matrices $\tilde{\mathbf{A}}_{p,\text{Rx}}^{(i)} = \mathbf{1}_N^\top \otimes \text{Diag}(\tilde{\mathbf{a}}_{p,\text{Rx}}^{(i)})$ and $\tilde{\mathbf{H}}_p^{(i)} = \tilde{\mathbf{h}}_p \mathbf{1}_{NM}^\top$, respectively, as well as the frequency matrix $\tilde{\mathbf{B}}_p^{(i)} = ((\tilde{\mathbf{c}}_p^{(i)})^\top \otimes (\tilde{\mathbf{G}}_{\text{Tx}}^{(i)})^\top) \otimes (\tilde{\mathbf{G}}_{\text{Rx}}^{(i)})^\top$ according to (9), the first approximate problem at iteration i is given by

$$\min_{\{\mathbf{a}_{p,\text{Tx}} \in \mathbb{C}^N\}_{p=1}^P} f_{\mathbf{a}_{\text{Tx}}} \left(\{\mathbf{a}_{p,\text{Tx}}, \tilde{\mathbf{a}}_{p,\text{Rx}}, \tilde{\mathbf{c}}_p, \tilde{\mathbf{h}}_p\}_{p=1}^P, \{\tilde{\mathbf{g}}_{n,\text{Tx}}\}_{n=1}^N, \{\tilde{\mathbf{g}}_{m,\text{Rx}}\}_{m=1}^M \right), \tag{18}$$

where we use the mode-one unfolding on (16) as defined in (12a) to obtain the cost function $f_{\mathbf{a}_{\text{Tx}}}(\{\mathbf{a}_{p,\text{Tx}}, \tilde{\mathbf{a}}_{p,\text{Rx}}, \tilde{\mathbf{c}}_p, \tilde{\mathbf{h}}_p\}_{p=1}^P, \{\tilde{\mathbf{g}}_{n,\text{Tx}}\}_{n=1}^N, \{\tilde{\mathbf{g}}_{m,\text{Rx}}\}_{m=1}^M) = \sum_{p=1}^P \|\mathbf{Y}_{p(1)} - (\text{Diag}(\mathbf{a}_{p,\text{Tx}}) \otimes \mathbf{1}_N^\top) (\tilde{\mathbf{H}}_p^{(i)} \otimes \tilde{\mathbf{B}}_p^{(i)} \otimes \tilde{\mathbf{A}}_{p,\text{Rx}}^{(i)})^\top\|_F^2$. Eventually, problem (18) can be separated into PN scalar subproblems

$$\min_{\{\mathbf{a}_{p,\text{Tx}}\}_n \in \mathbb{C}} \sum_{m=1}^M \left\| [\mathbf{y}_p]_{n,m,:} - [\mathbf{a}_{p,\text{Tx}}]_n [\tilde{\mathbf{a}}_{p,\text{Rx}}^{(i)}]_m \tilde{\mathbf{b}}_{n,m,p}^{(i)} (\tilde{\mathbf{h}}_p^{(i)})^\top \right\|_2^2 \tag{19}$$

$$\begin{aligned}
& \text{for } \tilde{\mathbf{b}}_{n,m,p}^{(i)} = (\tilde{\mathbf{c}}_p^{(i)} \otimes \tilde{\mathbf{g}}_{n,\text{Tx}}^{(i)} \otimes \tilde{\mathbf{g}}_{m,\text{Rx}}^{(i)}) \text{ with solutions} \\
& [\mathbf{a}_{p,\text{Tx}}^{(i+1)}]_n = \frac{\sum_{m=1}^M [\tilde{\mathbf{a}}_{p,\text{Rx}}^{(i)}]_m^* (\tilde{\mathbf{b}}_{n,m,p}^{(i)})^H [\mathbf{y}_p]_{n,m,:} (\tilde{\mathbf{h}}_p^{(i)})^*}{\|\tilde{\mathbf{h}}_p^{(i)}\|_2^2 \sum_{m=1}^M \left\| [\tilde{\mathbf{a}}_{p,\text{Rx}}^{(i)}]_m \right\|_2^2 \|\tilde{\mathbf{b}}_{n,m,p}^{(i)}\|_2^2} \tag{20}
\end{aligned}$$

for $n = 1, \dots, N$ and $p = 1, \dots, P$, respectively, that can be solved in parallel.

3.2. Update of $\{\mathbf{a}_{p,\text{Rx}}\}_{p=1}^P$

Similar to the update of $\{\mathbf{a}_{p,\text{Tx}}\}_{p=1}^P$, learning the receive steering vectors $\{\mathbf{a}_{p,\text{Rx}}\}_{p=1}^P$ requires solving the approximate problem in which all remaining parameters are fixed. At first, we again relax the constraints (15d) and (15e), which can always be satisfied by the proposed rescaling (17).

Using the mode-two unfolding in (12b) on (16), the approximate problem at iteration i is given by

$$\min_{\{\mathbf{a}_{p,\text{Rx}} \in \mathbb{C}^M\}_{p=1}^P} f_{\mathbf{a}_{\text{Rx}}} \left(\{\mathbf{a}_{p,\text{Rx}}, \mathbf{a}_{p,\text{Tx}}^{(i+1)}, \tilde{\mathbf{c}}_p, \tilde{\mathbf{h}}_p\}_{p=1}^P, \{\tilde{\mathbf{g}}_{n,\text{Tx}}\}_{n=1}^N, \{\tilde{\mathbf{g}}_{m,\text{Rx}}\}_{m=1}^M \right) \tag{21}$$

with $f_{\mathbf{a}_{\text{Rx}}}(\{\mathbf{a}_{p,\text{Rx}}, \mathbf{a}_{p,\text{Tx}}^{(i+1)}, \tilde{\mathbf{c}}_p, \tilde{\mathbf{h}}_p\}_{p=1}^P, \{\tilde{\mathbf{g}}_{n,\text{Tx}}\}_{n=1}^N, \{\tilde{\mathbf{g}}_{m,\text{Rx}}\}_{m=1}^M) = \sum_{p=1}^P \|\mathbf{Y}_{p(2)} - (\mathbf{1}_N^\top \otimes \text{Diag}(\mathbf{a}_{p,\text{Tx}}^{(i+1)})) (\mathbf{A}_{p,\text{Tx}}^{(i+1)} \otimes \tilde{\mathbf{H}}_p^{(i)} \otimes \tilde{\mathbf{B}}_p^{(i)})^\top\|_F^2$. Following the same steps as in Section 3.1, problem (21) is decoupled into PM scalar subproblems

$$\min_{\{\mathbf{a}_{p,\text{Rx}}\}_m \in \mathbb{C}} \sum_{n=1}^N \left\| [\mathbf{y}_p]_{n,m,:} - [\mathbf{a}_{p,\text{Rx}}]_m [\mathbf{a}_{p,\text{Tx}}^{(i+1)}]_n \tilde{\mathbf{b}}_{n,m,p}^{(i)} (\tilde{\mathbf{h}}_p^{(i)})^\top \right\|_2^2 \tag{22}$$

with solutions

$$[\mathbf{a}_{p,\text{Rx}}^{(i+1)}]_m = \frac{\sum_{n=1}^N [\mathbf{a}_{p,\text{Tx}}^{(i+1)}]_n^* (\tilde{\mathbf{b}}_{n,m,p}^{(i)})^H [\mathbf{y}_p]_{n,m,:} (\tilde{\mathbf{h}}_p^{(i)})^*}{\|\tilde{\mathbf{h}}_p^{(i)}\|_2^2 \sum_{n=1}^N \left\| [\mathbf{a}_{p,\text{Tx}}^{(i+1)}]_n \right\|_2^2 \|\tilde{\mathbf{b}}_{n,m,p}^{(i)}\|_2^2} \tag{23}$$

for $m = 1, \dots, M$ and $p = 1, \dots, P$.

3.3. Update of $\{\mathbf{c}_p\}_{p=1}^P$

Following the BCD procedure as above, we next consider the update of the block variables $\{\mathbf{c}_p\}_{p=1}^P$. First, we make the nonconvex constraint (15g) implicit by introducing the parameterization $[c_p]_\ell = e^{j\phi_{\ell,p}}$ and consider $\phi_{\ell,p}$ with $\phi_{\ell,p} \in [-\pi, \pi)$ for $\ell = 1, \dots, L$ and $p = 1, \dots, P$ as the optimization variables instead. Second, we relax constraint (15f), which can always be satisfied by the rescaling procedure (17).

Applying the mode-three unfolding in (12c) on (16) yields the modified approximate problem

$$\min_{\{\phi_p \in (-\pi, \pi)^L\}_{p=1}} f_\phi \left(\left\{ \phi_p, \mathbf{a}_{p,\text{Tx}}^{(i+1)}, \mathbf{a}_{p,\text{Rx}}^{(i+1)}, \tilde{\mathbf{h}}_p^{(i)} \right\}_{p=1}^P, \left\{ \tilde{\mathbf{g}}_{n,\text{Tx}}^{(i)} \right\}_{n=1}^N, \left\{ \tilde{\mathbf{g}}_{m,\text{Rx}}^{(i)} \right\}_{m=1}^M \right), \quad (24)$$

where $\phi_p = [\phi_{1,p}, \dots, \phi_{L,p}]^\top \in [-\pi, \pi]^L$ and $f_\phi(\{\phi_p, \mathbf{a}_{p,\text{Tx}}^{(i+1)}, \mathbf{a}_{p,\text{Rx}}^{(i+1)}, \tilde{\mathbf{h}}_p^{(i)}\}_{p=1}^P, \{\tilde{\mathbf{g}}_{n,\text{Tx}}^{(i)}\}_{n=1}^N, \{\tilde{\mathbf{g}}_{m,\text{Rx}}^{(i)}\}_{m=1}^M) = \sum_{p=1}^P \left\| \mathbf{Y}_{p(3)} - \text{Diag}(e^{j\phi_p}) \tilde{\mathbf{G}}^{(i)} (\mathbf{A}_{p,\text{Rx}}^{(i+1)} \otimes \mathbf{A}_{p,\text{Tx}}^{(i+1)} \otimes \tilde{\mathbf{H}}_p^{(i)})^\top \right\|_F^2$ using $\tilde{\mathbf{G}}^{(i)} = (\tilde{\mathbf{G}}_{\text{Tx}}^{(i)\top} \otimes \tilde{\mathbf{G}}_{\text{Rx}}^{(i)\top})^\top = [\text{Diag}(\tilde{\mathbf{g}}_{1,\text{Tx}}^{(i)}) \tilde{\mathbf{G}}_{\text{Rx}}^{(i)}, \dots, \text{Diag}(\tilde{\mathbf{g}}_{N,\text{Tx}}^{(i)}) \tilde{\mathbf{G}}_{\text{Rx}}^{(i)}]$ with $\tilde{\mathbf{G}}_{\text{Tx}}^{(i)}$ and $\tilde{\mathbf{G}}_{\text{Rx}}^{(i)}$ according to (10) and (11), respectively, while $e^{(\cdot)}$ denotes the elementwise exponential function.

As in Sections 3.1 and 3.2, problem (24) decouples and can be solved separately for every p . Additionally, the diagonal matrix containing the optimization variable, i.e. $\text{Diag}(e^{j\phi_p})$, decouples the optimization variable elements $[\phi_p]_\ell$, leading to PL parallel surrogate problems

$$\max_{\phi_{\ell,p} \in (-\pi, \pi)} \text{Re} \left(\left[\mathbf{Y}_{p(3)} \right]_{\ell,:}^\top \left(\mathbf{A}_{p,\text{Rx}}^{(i+1)} \otimes \mathbf{A}_{p,\text{Tx}}^{(i+1)} \otimes \tilde{\mathbf{H}}_p^{(i)} \right)^* \left[\tilde{\mathbf{G}}^{(i)} \right]_{\ell,:} e^{-j\phi_{\ell,p}} \right) \quad (25)$$

for $\ell = 1, \dots, L$ and $p = 1, \dots, P$, respectively. A maximizer to (25) is given by $\phi_{\ell,p}^{\text{opt}} = \arg(\left[\mathbf{Y}_{p(3)} \right]_{\ell,:}^\top (\mathbf{A}_{p,\text{Rx}}^{(i+1)} \otimes \mathbf{A}_{p,\text{Tx}}^{(i+1)} \otimes \tilde{\mathbf{H}}_p^{(i)})^* (\left[\tilde{\mathbf{G}}^{(i)} \right]_{\ell,:})^*)$ such that the ℓ th element of the phase response c_p can be estimated as

$$\begin{aligned} \left[c_p^{(i+1)} \right]_\ell &= e^{j\phi_{\ell,p}^{\text{opt}}} \\ &= e^{j \arg \left(\sum_{n=1}^N \sum_{m=1}^M \left[a_{p,\text{Tx}}^{(i+1)} \right]_n^* \left[a_{p,\text{Rx}}^{(i+1)} \right]_m \left[\tilde{\mathbf{g}}_{n,\text{Tx}}^{(i)} \right]_\ell \left[\tilde{\mathbf{g}}_{m,\text{Rx}}^{(i)} \right]_\ell \left(\tilde{\mathbf{h}}_p^{(i)} \right)^H \left[\mathbf{y}_p \right]_{n,m,\ell} \right)} \end{aligned} \quad (26)$$

for $\ell = 1, \dots, L$ and $p = 1, \dots, P$.

3.4. Update of $\{\mathbf{g}_{n,\text{Tx}}\}_{n=1}^N$

According to the BCD procedure, we next consider the block variable update $\{\mathbf{g}_{n,\text{Tx}}\}_{n=1}^N$. We relax the nonconvex constraint (15j) and consider $[\mathbf{g}_{n,\text{Tx}}]_\ell \leq 1$ for $n = 2, \dots, N$ and $\ell = 1, \dots, L$ instead, because the original constraint can always be satisfied by applying the rescaling (17) to the solution of the relaxed subproblem. The modified relaxed problem with the remaining parameters fixed therefore reduces to

$$\min_{\{\mathbf{g}_{n,\text{Tx}} \in \mathbb{R}_+^L\}_{n=1}} f_{\mathbf{g}_{\text{Tx}}} \left(\left\{ \mathbf{g}_{n,\text{Tx}} \right\}_{n=1}^N, \left\{ \mathbf{a}_{p,\text{Tx}}^{(i+1)}, \mathbf{a}_{p,\text{Rx}}^{(i+1)}, c_p^{(i+1)}, \tilde{\mathbf{h}}_p^{(i)} \right\}_{p=1}^P, \left\{ \tilde{\mathbf{g}}_{m,\text{Rx}}^{(i)} \right\}_{m=1}^M \right) \quad (27a)$$

$$\text{s.t.} \quad \mathbf{g}_{1,\text{Tx}} = \mathbf{1}_L, \quad (27b)$$

$$-[\mathbf{g}_{n,\text{Tx}}]_\ell + \varepsilon \leq 0, \quad n = 2, \dots, N, \ell = 1, \dots, L, \quad (27c)$$

$$[\mathbf{g}_{n,\text{Tx}}]_\ell - 1 \leq 0, \quad n = 2, \dots, N, \ell = 1, \dots, L, \quad (27d)$$

where we remark that $f_{\mathbf{g}_{\text{Tx}}}(\{\mathbf{g}_{n,\text{Tx}}\}_{n=1}^N, \{\mathbf{a}_{p,\text{Tx}}^{(i+1)}, \mathbf{a}_{p,\text{Rx}}^{(i+1)}, c_p^{(i+1)}, \tilde{\mathbf{h}}_p^{(i)}\}_{p=1}^P, \{\tilde{\mathbf{g}}_{m,\text{Rx}}^{(i)}\}_{m=1}^M) = \sum_{p=1}^P \sum_{n=1}^N \sum_{m=1}^M \sum_{\ell=1}^L \left\| \left[c_p^{(i+1)} \right]_\ell^* \left[\mathbf{y}_p \right]_{n,m,\ell} - [\mathbf{g}_{n,\text{Tx}}]_\ell \left[\tilde{\mathbf{g}}_{m,\text{Rx}}^{(i)} \right]_\ell \left[a_{p,\text{Tx}}^{(i+1)} \right]_n \left[a_{p,\text{Rx}}^{(i+1)} \right]_m \tilde{\mathbf{h}}_p^{(i)} \right\|_F^2$ takes measurements from all P positions into account.

Ignoring the constraints in (27c)–(27d), the problem reduces to a simple linear LS problem with decoupled variables. The corresponding minimizers are given in closed form as

$$\left[\mathbf{g}_{n,\text{Tx}}^{\text{LS}} \right]_\ell = \frac{\text{Re} \left(\sum_{p=1}^P \sum_{m=1}^M \left[a_{p,\text{Tx}}^{(i+1)} \right]_n^* \left[a_{p,\text{Rx}}^{(i+1)} \right]_m \left[c_p^{(i+1)} \right]_\ell^* \left[\tilde{\mathbf{g}}_{m,\text{Rx}}^{(i)} \right]_\ell \left(\tilde{\mathbf{h}}_p^{(i)} \right)^H \left[\mathbf{y}_p \right]_{n,m,\ell} \right)}{\sum_{p=1}^P \sum_{m=1}^M \left| \left[a_{p,\text{Tx}}^{(i+1)} \right]_n \right|^2 \left| \left[a_{p,\text{Rx}}^{(i+1)} \right]_m \right|^2 \left(\left[\tilde{\mathbf{g}}_{m,\text{Rx}}^{(i)} \right]_\ell \right)^2 \left\| \tilde{\mathbf{h}}_p^{(i)} \right\|_2^2} \quad (28)$$

for $\ell = 1, \dots, L$ and $n = 2, \dots, N$. Neglecting the trivial case of $n = 1$, there remain $L(N-1)$ terms in (27a) that are quadratic functions in one scalar variable each, such that there exists a respective global minimum that either fulfills (27c)–(27d) or is located outside these boundaries. In the latter case, (27a) is strictly monotonically descending towards (28) within the constrained interval. The solution to (27) is therefore given by (28) projected onto $[\varepsilon, 1]$, i.e.,

$$\left[\mathbf{g}_{n,\text{Tx}}^{(i+1)} \right]_\ell = \begin{cases} 1 & [\mathbf{g}_{n,\text{Tx}}^{\text{LS}}]_\ell > 1 \\ [\mathbf{g}_{n,\text{Tx}}^{\text{LS}}]_\ell & \varepsilon \leq [\mathbf{g}_{n,\text{Tx}}^{\text{LS}}]_\ell \leq 1 \\ \varepsilon & [\mathbf{g}_{n,\text{Tx}}^{\text{LS}}]_\ell < \varepsilon. \end{cases} \quad (29)$$

3.5. Update of $\{\mathbf{g}_{m,\text{Rx}}\}_{m=1}^M$

Following similar considerations as in the previous subsection, we relax the nonconvex constraint (15l) by considering $[\mathbf{g}_{m,\text{Rx}}]_\ell \leq 1$ for $m = 1, \dots, M$ and $\ell = 1, \dots, L$ instead, and remark that the original constraint can always be satisfied by proper rescaling of the solution of the relaxed subproblem according to (17).

The resulting relaxed problem is

$$\min_{\{\mathbf{g}_{m,\text{Rx}} \in \mathbb{R}_+^L\}_{m=1}} f_{\mathbf{g}_{\text{Rx}}} \left(\left\{ \mathbf{g}_{m,\text{Rx}} \right\}_{m=1}^M, \left\{ \mathbf{a}_{p,\text{Tx}}^{(i+1)}, \mathbf{a}_{p,\text{Rx}}^{(i+1)}, c_p^{(i+1)}, \tilde{\mathbf{h}}_p^{(i)} \right\}_{p=1}^P, \left\{ \mathbf{g}_{n,\text{Tx}}^{(i+1)} \right\}_{n=1}^N \right) \quad (30a)$$

$$\text{s.t.} \quad -[\mathbf{g}_{m,\text{Rx}}]_\ell + \varepsilon \leq 0, \quad m = 1, \dots, M, \ell = 1, \dots, L, \quad (30b)$$

$$[\mathbf{g}_{m,\text{Rx}}]_\ell - 1 \leq 0, \quad m = 1, \dots, M, \ell = 1, \dots, L \quad (30c)$$

with $f_{\mathbf{g}_{\text{Rx}}}(\{\mathbf{g}_{m,\text{Rx}}\}_{m=1}^M, \{\mathbf{a}_{p,\text{Tx}}^{(i+1)}, \mathbf{a}_{p,\text{Rx}}^{(i+1)}, c_p^{(i+1)}, \tilde{\mathbf{h}}_p^{(i)}\}_{p=1}^P, \{\mathbf{g}_{n,\text{Tx}}^{(i+1)}\}_{n=1}^N) = \sum_{p=1}^P \sum_{n=1}^N \sum_{m=1}^M \sum_{\ell=1}^L \left\| \left[c_p^{(i+1)} \right]_\ell^* \left[\mathbf{y}_p \right]_{n,m,\ell} - [\mathbf{g}_{m,\text{Rx}}]_\ell \left[\mathbf{g}_{n,\text{Tx}}^{(i+1)} \right]_\ell \left[a_{p,\text{Tx}}^{(i+1)} \right]_n \left[a_{p,\text{Rx}}^{(i+1)} \right]_m \tilde{\mathbf{h}}_p^{(i)} \right\|_2^2$.

The corresponding LS solution of the relaxed problem is given by

$$\left[\mathbf{g}_{m,\text{Rx}}^{\text{LS}} \right]_\ell = \frac{\text{Re} \left(\sum_{p=1}^P \sum_{n=1}^N \left[a_{p,\text{Tx}}^{(i+1)} \right]_n^* \left[a_{p,\text{Rx}}^{(i+1)} \right]_m \left[c_p^{(i+1)} \right]_\ell^* \left[\mathbf{g}_{n,\text{Tx}}^{(i+1)} \right]_\ell \left(\tilde{\mathbf{h}}_p^{(i)} \right)^H \left[\mathbf{y}_p \right]_{n,m,\ell} \right)}{\sum_{p=1}^P \sum_{n=1}^N \left| \left[a_{p,\text{Tx}}^{(i+1)} \right]_n \right|^2 \left| \left[a_{p,\text{Rx}}^{(i+1)} \right]_m \right|^2 \left(\left[\mathbf{g}_{n,\text{Tx}}^{(i+1)} \right]_\ell \right)^2 \left\| \tilde{\mathbf{h}}_p^{(i)} \right\|_2^2} \quad (31)$$

for $\ell = 1, \dots, L$ and $m = 1, \dots, M$, which are again projected onto $[\varepsilon, 1]$, i.e.,

$$\left[\mathbf{g}_{m,\text{Rx}}^{(i+1)} \right]_\ell = \begin{cases} 1 & [\mathbf{g}_{m,\text{Rx}}^{\text{LS}}]_\ell > 1 \\ [\mathbf{g}_{m,\text{Rx}}^{\text{LS}}]_\ell & \varepsilon \leq [\mathbf{g}_{m,\text{Rx}}^{\text{LS}}]_\ell \leq 1 \\ \varepsilon & [\mathbf{g}_{m,\text{Rx}}^{\text{LS}}]_\ell < \varepsilon. \end{cases} \quad (32)$$

3.6. Update of $\{\mathbf{h}_p\}_{p=1}^P$

Making use of the definitions (13a), (13b), and (9), the approximate problem in the gain vectors $\{\mathbf{h}_p\}_{p=1}^P$ for the remaining parameters fixed yields the standard linear LS problem

$$\min_{\{\mathbf{h}_p \in \mathbb{C}^T\}_{p=1}} f_{\mathbf{h}} \left(\left\{ \mathbf{h}_p, \mathbf{a}_{p,\text{Tx}}^{(i+1)}, \mathbf{a}_{p,\text{Rx}}^{(i+1)}, c_p^{(i+1)} \right\}_{p=1}^P, \left\{ \mathbf{g}_{n,\text{Tx}}^{(i+1)} \right\}_{n=1}^N, \left\{ \mathbf{g}_{m,\text{Rx}}^{(i+1)} \right\}_{m=1}^M \right) \quad (33)$$

with $f_{\mathbf{h}}(\{\mathbf{h}_p, \mathbf{a}_{p,\text{Tx}}^{(i+1)}, \mathbf{a}_{p,\text{Rx}}^{(i+1)}, c_p^{(i+1)}\}_{p=1}^P, \{\mathbf{g}_{n,\text{Tx}}^{(i+1)}\}_{n=1}^N, \{\mathbf{g}_{m,\text{Rx}}^{(i+1)}\}_{m=1}^M) = \sum_{p=1}^P \left\| \mathbf{Y}_{p(4)} - \mathbf{h}_p \mathbf{1}_{NM}^\top (\mathbf{B}_p^{(i+1)} \otimes \mathbf{A}_{p,\text{Rx}}^{(i+1)} \otimes \mathbf{A}_{p,\text{Tx}}^{(i+1)})^\top \right\|_F^2$. The problem (33) decouples into P LS problems with individual minimizers given by

$$\mathbf{h}_p^{(i+1)} = \frac{\sum_{n=1}^N \sum_{m=1}^M \left[a_{p,\text{Tx}}^{(i+1)} \right]_n^* \left[a_{p,\text{Rx}}^{(i+1)} \right]_m \left(\left[\mathbf{y}_p \right]_{n,m,\cdot} \right)^\top \left(\mathbf{b}_{n,m,p}^{(i+1)} \right)^*}{\sum_{n=1}^N \sum_{m=1}^M \left| \left[a_{p,\text{Tx}}^{(i+1)} \right]_n \right|^2 \left| \left[a_{p,\text{Rx}}^{(i+1)} \right]_m \right|^2 \left\| \mathbf{b}_{n,m,p}^{(i+1)} \right\|_2^2} \quad (34)$$

for $p = 1, \dots, P$. After the update of $\{\mathbf{h}_p\}_{p=1}^P$, iteration i concludes by initiating the scaling procedure (17).

With this, we now have introduced the subproblems and corresponding solutions of a modified BCD method to learn the array response for P sample calibration points by estimating the corresponding parameters of the tensor model in (3), i.e. $\{\mathbf{g}_{n,\text{Tx}}\}_{n=1}^N$, $\{\mathbf{g}_{m,\text{Rx}}\}_{m=1}^M$, and $\{\mathbf{a}_{p,\text{Tx}}, \mathbf{a}_{p,\text{Rx}}, \mathbf{c}_p, \mathbf{h}_p\}_{p=1}^P$. Additionally, the solutions to all approximate problems of the modified BCD method are given in closed-form and the individual block variables as well as their rescaling (17) can be computed in parallel.

3.7. Initialization of the BCD

The parameter $\mathbf{g}_{1,\text{Tx}}$ is fixed according to (15h), so w.l.o.g., we start our proposed calibration procedure by estimating the transmit magnitude response update $\mathbf{g}_{n,\text{Tx}}^{(i+1)}$ at iteration i . Estimates for the remaining parameters at the initial iteration $i = 1$ are obtained from the calibration data for snapshots $t = 1, \dots, T$ using the simple initialization $\tilde{\mathbf{a}}_{p,\text{Tx}}^{(1)} = \mathbf{1}_N$, $\tilde{\mathbf{a}}_{p,\text{Rx}}^{(1)} = \mathbf{1}_M$, $\tilde{\mathbf{g}}_{m,\text{Rx}}^{(1)} = \mathbf{1}_L$, $\tilde{\mathbf{c}}_p^{(1)} = \mathbf{1}_L$, and $[\tilde{\mathbf{h}}_p^{(1)}]_t = (LMN)^{-1} \sum_{\ell=1}^L \sum_{m=1}^M \sum_{n=1}^N |\text{Re}(\{\mathcal{Y}_p\}_{n,m,\ell,t})| + j(LMN)^{-1} \sum_{\ell=1}^L \sum_{m=1}^M \sum_{n=1}^N |\text{Im}(\{\mathcal{Y}_p\}_{n,m,\ell,t})|$, which we denote as the complex-valued t -average (t -av). These initial estimates can be obtained from the measurements in \mathcal{Y}_p without additional knowledge of the calibration positions p .

3.8. Range scanning

Our experiments reveal that the phase responses $\{\mathbf{c}_p\}_{p=1}^P \in \mathbb{C}^L$ learned from calibration measurements exhibit approximately linear phases that are distant-dependent. Thus, we conclude that the far field model with constant group delays holds [67]. Hence, we may model the entries of the p th phase response as

$$[c_p]_{\ell} = e^{-j(\ell-1)\Delta\phi_p} \quad (35)$$

with phase slope $\Delta\phi_p = 2(r_p + r_0)\frac{\Delta\omega}{c}$, where c is the effective speed of sound for the imaging burst, r_p is the adjusted range from the array to the calibration target position indexed by p , r_0 is a system offset, e.g. due to unknown group delays introduced by the waveguide and mechanical inertia of the PUTs, and $\Delta\omega = 2\pi f_s(L_{\text{DFT}})^{-1}$ is the radial frequency separation based on the sampling frequency f_s as well as the DFT length L_{DFT} .

While the true range r_p is known for every calibration point p , the system offset range r_0 is generally unknown. However, we can determine r_0 using the estimation of signal parameters via rotational invariance technique (ESPRIT) for the simple case of a single source as [68]

$$\hat{r}_0 = \frac{c}{2\Delta\omega} \sum_{p=1}^P \left(\arg([\hat{c}_p]_{1:L-1}^H [\hat{c}_p]_{2:L}) - 2r_p \frac{\Delta\omega}{c} \right). \quad (36)$$

With the model-based approach described above, the density of dictionary entries in the range dimension can be flexibly increased by choosing different scanning ranges $r'_{p_1}, \dots, r'_{p_R}$ for every calibrated position p . Thus, the total number of dictionary entries P is increased to $P = RP_{\text{measured}}$. This allows a higher accuracy for the estimation of the range in distances that have not been learned during calibration.

3.9. Complexity and methods for comparison

Instead of learning from measurements under the common narrow-band assumption [53], a normalized and single-snapshot array response $\mathcal{R}_p \in \mathbb{C}^{M \times N \times L}$ for a single target at position p can be described in closed form as the third-order tensor

$$\mathcal{R}_{p,\text{analytic}} = \mathbf{a}_{p,\text{Tx},\text{analytic}} \circ \mathbf{a}_{p,\text{Rx},\text{analytic}} \circ \mathbf{b}_{p,\text{analytic}} \quad (37)$$

using the analytic steering vectors $\mathbf{a}_{p,\text{Tx},\text{analytic}} = [e^{-jk(\theta,\varphi)^T \mathbf{r}_{1,\text{Tx}}}, \dots, e^{-jk(\theta,\varphi)^T \mathbf{r}_{N,\text{Tx}}}]^T$ and $\mathbf{a}_{p,\text{Rx},\text{analytic}} = [e^{-jk(\theta,\varphi)^T \mathbf{r}_{1,\text{Rx}}}, \dots, e^{-jk(\theta,\varphi)^T \mathbf{r}_{M,\text{Rx}}}]^T$, the

Table 1

Computational load of multiply-accumulate (MAC) operations for different tensor-based calibration algorithms.

Algorithm	Computational load
Broadside compensation	$\mathcal{O}(P(N+M+L))$
Rank-1 CPD	$\mathcal{O}(PNMLT)$
Proposed	$\mathcal{O}(PNMLT)$

linear frequency response $\mathbf{b}_{p,\text{analytic}} = [1, \dots, e^{-j2(L-1)r_p \frac{\Delta\omega}{c}}]^T$, the wave vector $\mathbf{k}(\theta, \varphi) = -2\pi f_0 c^{-1} [\sin(\theta)\cos(\varphi), \sin(\varphi), \cos(\theta)\cos(\varphi)]^T$, the array element positions $\mathbf{r}_i = [x_i, y_i, z_i]^T$, and $\Delta\omega = 2\pi f_s(L_{\text{DFT}})^{-1}$. Note that the analytic frequency response $\mathbf{b}_{p,\text{analytic}}$ uses the same linear phase model as described in Section 3.8.

A simple calibration technique that reduces relative gain and phase offsets in the different transceiver elements is given by broadside compensation [53,69]. For this, a measurement tensor $\mathcal{Y}_{(0^\circ,0^\circ)}$ with a target at broadside direction $(\theta, \varphi) = (0^\circ, 0^\circ)$ is approximated by the rank-1 CPD (5) using a classic alternating least squares (ALS) algorithm [61] with the initialization in Section 3.7. After appropriate rescaling, unique estimates $\hat{\mathbf{a}}_{(0^\circ,0^\circ),\text{Tx},\text{CPD}}$, $\hat{\mathbf{a}}_{(0^\circ,0^\circ),\text{Rx},\text{CPD}}$, and $\hat{\mathbf{b}}_{(0^\circ,0^\circ),\text{CPD}}$ are used as complex valued gains, i.e. amplitude factors and phase shifts, to correct the components of the analytic array responses \mathcal{R}_p of all directions at the same range:

$$\begin{aligned} \mathbf{a}_{p,\text{Tx},\text{analytic}} &= \hat{\mathbf{a}}_{(0^\circ,0^\circ),\text{Tx},\text{CPD}} \odot \left[e^{-j\mathbf{k}(\theta,\varphi)^T \mathbf{r}_{1,\text{Tx}}}, \dots, e^{-j\mathbf{k}(\theta,\varphi)^T \mathbf{r}_{N,\text{Tx}}} \right]^T, \\ \mathbf{a}_{p,\text{Rx},\text{analytic}} &= \hat{\mathbf{a}}_{(0^\circ,0^\circ),\text{Rx},\text{CPD}} \odot \left[e^{-j\mathbf{k}(\theta,\varphi)^T \mathbf{r}_{1,\text{Rx}}}, \dots, e^{-j\mathbf{k}(\theta,\varphi)^T \mathbf{r}_{M,\text{Rx}}} \right]^T, \\ \mathbf{b}_{p,\text{analytic}} &= \hat{\mathbf{b}}_{(0^\circ,0^\circ),\text{CPD}} \odot \left[e^{-j2 \cdot 0 \cdot r_p \frac{\Delta\omega}{c}}, \dots, e^{-j2(L-1)r_p \frac{\Delta\omega}{c}} \right]^T. \end{aligned} \quad (38)$$

The analytic model for \mathcal{R}_p yields a low computational load with broadside compensation but requires precise knowledge of the array geometry, which may be unavailable if the array is embedded in a system or affected by temperature changes and aging. Our proposed calibration technique and the positionwise rank-1 CPD approximation (5) overcome this limitation, albeit with higher computational complexity.

The computational cost of the modified BCD procedure for problem (15) is mainly driven by updating the magnitude responses $\{\mathbf{g}_{n,\text{Tx}}\}_{n=1}^N$ and $\{\mathbf{g}_{m,\text{Rx}}\}_{m=1}^M$, which sets our tensor model apart from the rank-1 CPD approximation. As noted in Sections 3.4 and 3.5, estimating $\mathbf{g}_{n,\text{Tx}}$ and $\mathbf{g}_{m,\text{Rx}}$ requires measurements from all P positions, respectively. While this makes our method computationally more demanding than a positionwise rank-1 CPD approximation, the complexity remains in the same order as the decoupling of subproblems allows for elementwise updates. Table 1 lists the computational load for the three calibration techniques in terms of multiply-accumulate (MAC) operations, where the load for the rank-1 CPD approximation is based on elementwise updates for a fair comparison.

3.10. Convergence analysis

In the following, we establish the convergence result for the proposed modified BCD algorithm that follows the proof of the conventional BCD algorithm provided in [66, Proposition 3.7.1]. Let us define the vector $\boldsymbol{\theta}^{(i)}$ that contains all block variables $\{\mathbf{a}_{p,\text{Tx}}^{(i+1)}, \mathbf{a}_{p,\text{Rx}}^{(i+1)}, \boldsymbol{\phi}_p^{(i+1)}, \mathbf{h}_p^{(i+1)}\}_{p=1}^P$, $\{\mathbf{g}_{n,\text{Tx}}^{(i+1)}\}_{n=1}^N$, $\{\mathbf{g}_{m,\text{Rx}}^{(i+1)}\}_{m=1}^M$ at iteration i after performing their respective updates (20), (23), (26), (29), (32) and (34) but prior to the scaling, whereas $\tilde{\boldsymbol{\theta}}^{(i)}$ denotes the vector of all block variables $\{\tilde{\mathbf{a}}_{p,\text{Tx}}^{(i+1)}, \tilde{\mathbf{a}}_{p,\text{Rx}}^{(i+1)}, \tilde{\boldsymbol{\phi}}_p^{(i+1)}, \tilde{\mathbf{h}}_p^{(i+1)}\}_{p=1}^P$, $\{\tilde{\mathbf{g}}_{n,\text{Tx}}^{(i+1)}\}_{n=1}^N$, $\{\tilde{\mathbf{g}}_{m,\text{Rx}}^{(i+1)}\}_{m=1}^M$ at iteration i after the rescaling in (17). The following convergence result can then be established.

Proposition 1. *Every limit point of the sequence $\{\tilde{\theta}^{(i)}\}$ is a stationary point of problem (15).*

Sketch of Proof for Proposition 1. The above convergence statement can be justified by extending the proof of [66, Proposition 3.7.1] for the classic BCD algorithm. We first observe that in each block variable update, as well as in the scaling step, the function value is nonincreasing. As the objective is bounded below, it follows from the Monotone Convergence Theorem that the function values corresponding to the iterates converge. To further show that a limit point $\bar{\theta}$ of the sequence $\{\tilde{\theta}^{(i)}\}$ is a stationary point of problem (15), we follow the proof of [66, Proposition 3.7.1]. We first note that all respective subproblems, i.e. (19), (22), (25), (27), (30), and (33) have unique minimizers. The objective functions of the subproblems are continuously differentiable over the constraint sets and monotonically nonincreasing between the current iterates and the minimizers of the subproblems. Furthermore, the constraint sets are convex and bounded. Thus, the conditions in [66, Proposition 3.7.1] are satisfied. Performing the exact steps in the proof of [66, Proposition 3.7.1] along the chain of BCD updates in one iteration, we can demonstrate that every limit point $\bar{\theta}$ of the sequence of iterates $\{\tilde{\theta}^{(i)}\}$ satisfies the first-order stationarity condition

$$\text{Re}(\nabla f(\bar{\theta})^H(\theta - \bar{\theta})) \geq 0 \quad \forall \theta \in \Theta, \quad (39)$$

where $\nabla f(\bar{\theta})$ and Θ denote the vector of partial derivatives and the feasible set of the problem without scaling constraints, i.e., the set defined by constraints (27b), (27c), (27d), (30b), (30c), respectively. Together with the fact that the sequence of iterates $\{\tilde{\theta}^{(i)}\}$ is enforced to satisfy the scaling constraints by the scaling procedure (17), it can be concluded from (39) that every limit point $\bar{\theta}$ is a stationary point of problem (15). \square

Due to the multilinear nature of its objective, we note that problem (15) is nonconvex, and the convergence of the modified BCD algorithm to a global minimum cannot generally be guaranteed (c.f. [66]). Therefore, the stationary point to which the proposed modified BCD algorithm converges may be a global minimum, a local minimum, or a saddle point of problem (15).

4. Imaging

As pointed out in Section 1, air-coupled US uses the same image formation principles as other in-air sensing modalities. Basic but fast techniques, such as delay-and-sum beamforming in the time domain and conventional beamforming in the frequency domain, have been successfully applied to air-coupled ultrasonic arrays [54,70]. Advanced methods, e.g. multiple signal classification (MUSIC) [71] or ESPRIT [68], promise superresolution, provided the array is well-calibrated. Another class of imaging techniques leverages sparsity in the scene, which can be exploited using sparsity-promoting concepts, e.g. convex ℓ_1 -norm minimization [72], including the LASSO problem considered in our previous work [49]. Sequential algorithms, such as matching pursuit (MP), orthogonal matching pursuit (OMP), and orthogonal least squares (OLS) [73], exploit sparsity using a dictionary, which we obtain from calibration measurements. As a proof-of-concept that array responses can be learned from calibration data with the algorithm provided in Section 3, we employ a sequential multi-target estimation technique that estimates target locations one by one.

Consider the superposition of K sources according to our signal model in (3), i.e.,

$$\mathcal{Y} = \sum_{k=1}^K \mathcal{Y}_{p_k} = \sum_{k=1}^K \mathcal{Q}_{p_k} \circ \mathbf{h}_{p_k} + \mathcal{Z}, \quad (40)$$

where \mathcal{Y}_{p_k} models the single-source tensor (3) for the k th target at the unknown position indexed by p_k . The noiseless signal part contributed

by the k th target can be factorized into the signal gain \mathbf{h}_{p_k} and the third-order tensor

$$\mathcal{Q}_{p_k} = \sum_{n=1}^N \sum_{m=1}^M (\mathbf{e}_n \circ \mathbf{a}_{p,\text{Tx}}) \circ (\mathbf{e}_m \circ \mathbf{a}_{p,\text{Rx}}) \circ (\mathbf{g}_{n,\text{Tx}} \circ \mathbf{g}_{m,\text{Rx}} \circ \mathbf{c}_p) \in \mathbb{C}^{N \times M \times L} \quad (41)$$

that is formed from the factors $(\mathbf{a}_{p,\text{Tx}}, \mathbf{a}_{p,\text{Rx}}, \mathbf{c}_p, \mathbf{g}_{n,\text{Tx}}, \mathbf{g}_{m,\text{Rx}})$ for calibration points $p = 1, \dots, P$. The tensor \mathcal{Q}_{p_k} in (41) characterizes the array range-angular response of a point reflector at the candidate location indexed by p and is assumed to be fixed and known after calibration. Let

$$\mathbf{q}_p = \text{vec}(\mathcal{Q}_{p_k}) \in \mathbb{C}^{NML} \quad (42)$$

denote the vectorization of the array response tensor \mathcal{Q}_{p_k} at calibration position p and let the set

$$\mathcal{Q} = \{\mathbf{q}_1, \mathbf{q}_2, \dots, \mathbf{q}_P\} \quad (43)$$

denote the range-angle dictionary for P candidate targets. Our objective is to find the atoms $\mathbf{q}_{\hat{p}_k}$ in the sparse representation $\text{unf}_4(\mathcal{Y}) = \mathbf{Y}_{(4)} \approx \sum_{k=1}^K \hat{\mathbf{h}}_{p_k} \mathbf{q}_{\hat{p}_k}^T$ under the mode-four unfolding from (12d). We remark that the true source number K is generally unknown and needs to be detected [53].

4.1. Sequential imaging with OMP

We select the atoms for the sparse representation of the image measurement tensor \mathcal{Y} according to the OMP technique [74]. At the beginning of the i th iteration of OMP, the location estimate indices $\hat{p}_1, \dots, \hat{p}_{i-1}$ corresponding to the selected atoms $\mathbf{q}_{\hat{p}_1}, \dots, \mathbf{q}_{\hat{p}_{i-1}} \in \mathcal{Q}$ along with the corresponding signal gain estimate vectors $\hat{\mathbf{h}}_1^{(i-1)}, \dots, \hat{\mathbf{h}}_{i-1}^{(i-1)} \in \mathbb{C}^T$ of the previously estimated targets are given and the location index estimate \hat{p}_i of the target in the i th iteration is selected as the minimizer

$$\hat{p}_i = \arg \min_{p \in \{1, \dots, P\}} \min_{\mathbf{h} \in \mathbb{C}^T} \left\| \mathbf{Y}_{(4)} - \sum_{k=1}^{i-1} \hat{\mathbf{h}}_k^{(i-1)} \mathbf{q}_{\hat{p}_k}^T - \mathbf{h} \mathbf{q}_p^T \right\|_F^2. \quad (44)$$

The inner optimization problem in (44) is a linear LS problem in \mathbf{h} for fixed \mathbf{q}_p and has the closed form solution $\mathbf{h}^{\text{LS}} = (\mathbf{Y}_{(4)} - \sum_{k=1}^{i-1} \hat{\mathbf{h}}_k^{(i-1)} \mathbf{q}_{\hat{p}_k}^T) (\|\mathbf{q}_p\|_2^2)^{-1} \mathbf{q}_p^*$. Inserting \mathbf{h}^{LS} for \mathbf{h} in (44) yields the simple selection criterion

$$\text{Step 1:} \quad \hat{p}_i = \arg \max_{p \in \{1, \dots, P\}} \left\| \mathbf{Y}_{(4), \text{res.}}^{(i-1)} \frac{\mathbf{q}_p^*}{\|\mathbf{q}_p\|_2} \right\|_2^2, \quad (45)$$

where

$$\mathbf{Y}_{(4), \text{res.}}^{(i-1)} = \mathbf{Y}_{(4)} - \sum_{k=1}^{i-1} \hat{\mathbf{h}}_k^{(i-1)} \mathbf{q}_{\hat{p}_k}^T \quad (46)$$

is the unfolded residual measurement tensor at the end of the $(i-1)$ th iteration. At the i th iteration, we observe that according to (45), the atom \mathbf{q}_p of our learned dictionary \mathcal{Q} is selected that has the largest correlation to the rows of the residual in (46).

In the second step of the i th iteration of the OMP method, all gain vectors $\{\hat{\mathbf{h}}_k^{(i)}\}_{k=1}^i$ corresponding to the selected target directions $\{\hat{p}_k\}_{k=1}^i$ are estimated for fixed atoms $\{\mathbf{q}_{\hat{p}_k}^{(i)}\}_{k=1}^i$ as the LS minimizers

$$\text{Step 2:} \quad \hat{\mathbf{h}}_k^{(i)} = \arg \min_{\mathbf{h} \in \mathbb{C}^T} \left\| \mathbf{Y}_{(4)} - \sum_{k=1}^i \mathbf{h}_k \mathbf{q}_{\hat{p}_k}^T \right\|_F^2 \\ = \left[\mathbf{Y}_{(4)} (\hat{\mathbf{Q}}^{(i)})^* \left((\hat{\mathbf{Q}}^{(i)})^T (\hat{\mathbf{Q}}^{(i)})^{-1} \right)^{-1} \right]_{:,k}, \quad (47)$$

where $\hat{\mathbf{Q}}^{(i)} = [\mathbf{q}_{\hat{p}_1}, \dots, \mathbf{q}_{\hat{p}_i}]$. We remark that $\|\hat{\mathbf{h}}_k\|_2^2$, which is a measure for the received power of the signal reflected by the target detected at the position indexed by k , is later used to create the image.

The two steps of the OMP procedure are repeated, e.g., until the Frobenius norm of the updated unfolded residual measurement tensor $\mathbf{Y}_{(4),\text{res}}^{(i)}$ according to (46) falls below a predefined threshold η , i.e. $\|\mathbf{Y}_{(4),\text{res}}^{(i)}\|_F^2 \leq \eta$, or a maximum number of iterations I_{OMP} is reached.

5. Results and discussion

In this section, we carry out numerical experiments to investigate the error performance of the proposed calibration technique and its impact on the imaging quality using both synthetic and real measurements recorded with an air-coupled ultrasonic array [54].

5.1. Simulations

We first evaluate our proposed modified BCD method for tensor-based array calibration with synthetic data from $P = 250$ different calibration points, $N = 4$ transmit and $M = 60$ receive elements, $L = 24$ DFT bins, and $T = 10$ snapshots. We model the transmit steering vector element $[\mathbf{a}_{p,\text{Tx}}]_n$, the receive steering vector element $[\mathbf{a}_{p,\text{Rx}}]_m$, the phase response element $[c_p]_\ell$, and the pulse gain element $[h_p]$, as i.i.d. random variables with unit-magnitude and uniform random phase in $[-\pi, \pi]$, for $p = 1, \dots, P$, $n = 1, \dots, N$, $m = 1, \dots, M$, $\ell = 1, \dots, L$, and $t = 1, \dots, T$. The transmit magnitude response element $[\mathbf{g}_{n,\text{Tx}}]_\ell$ and the receive magnitude response element $[\mathbf{g}_{m,\text{Rx}}]_\ell$ are uniformly drawn from $[1 - \delta, 1]$, with $0 \leq \delta < 1$ modeling variations among transmitters and receivers and $\delta = 0$ corresponding to identical frequency responses. Simulations at varying SNR levels are performed using the tensor factorization according to (3), where we assume i.i.d. zero-mean complex circular Gaussian noise.

We use the MCNCC of each estimated range-angle dictionary entry in (42) as a performance metric that is to a large extent independent of existing scaling ambiguities. In a Monte Carlo simulation with I_{MC} Monte Carlo trials, the MCNCC is defined as

$$\text{MCNCC} = \frac{1}{I_{\text{MC}} P} \sum_{i_{\text{MC}}=1}^{I_{\text{MC}}} \sum_{p=1}^P \left(1 - \frac{|\mathbf{q}_{p,i_{\text{MC}}}^H \hat{\mathbf{q}}_{p,i_{\text{MC}}}|}{\|\mathbf{q}_{p,i_{\text{MC}}}\|_2 \|\hat{\mathbf{q}}_{p,i_{\text{MC}}}\|_2} \right), \quad (48)$$

where $\mathbf{q}_{p,i_{\text{MC}}}$ and $\hat{\mathbf{q}}_{p,i_{\text{MC}}}$ are the vectorized range-angle responses of the true parameter values $\{\mathbf{g}_{n,\text{Tx}}\}_{n=1}^N$, $\{\mathbf{g}_{m,\text{Rx}}\}_{m=1}^M$, and $\{\mathbf{a}_{p,\text{Tx}}, \mathbf{a}_{p,\text{Rx}}, c_p\}_{p=1}^P$ and the corresponding finite iteration parameter estimates $\{\hat{\mathbf{g}}_{n,\text{Tx}}\}_{n=1}^N$, $\{\hat{\mathbf{g}}_{m,\text{Rx}}\}_{m=1}^M$, and $\{\hat{\mathbf{a}}_{p,\text{Tx}}, \hat{\mathbf{a}}_{p,\text{Rx}}, \hat{c}_p\}_{p=1}^P$ at the termination of the modified BCD algorithm for $p = 1, \dots, P$, $n = 1, \dots, N$ and $m = 1, \dots, M$, respectively, according to (41) and (42). In terms of coherence [75], we remark that the MCNCC is inversely proportional to the coherence between $\mathbf{q}_{p,i_{\text{MC}}}$ and $\hat{\mathbf{q}}_{p,i_{\text{MC}}}$, i.e., the MCNCC is zero for full coherence and one for full incoherence.

In Fig. 3, the MCNCC metric is averaged over $I_{\text{MC}} = 100$ Monte Carlo trials after each decomposition reaches $f_{\text{rel}}^{(i-1)} - f_{\text{rel}}^{(i)} \leq 10^{-6}$, where

$$f_{\text{rel}}^{(i)} = \left(\sum_{p=1}^P \|\mathbf{y}_p\|_F^2 \right)^{-1} \sum_{p=1}^P \|\mathbf{y}_p - \hat{\mathbf{y}}_p^{(i)}\|_F^2 \quad (49)$$

is the normalized cost function (16) at the i th iteration of our proposed modified BCD procedure. We compare the MCNCC for $\delta \in \{0, 0.1, 0.5\}$ to illustrate the influence of transmitters and receivers with increasingly different frequency responses. With our proposed method, the MCNCC converges to 0, i.e. full coherence between \mathbf{q}_p and $\hat{\mathbf{q}}_p$, with rising SNR, regardless of the distortion parameter δ . For identical frequency responses, i.e. $\delta = 0$, the data can well be approximated with a rank-1 CPD introduced in Section 3.9. For $\delta > 0$, however, i.e. nonidentical frequency responses of individual transducers, a rank-1 CPD is unsuitable as the MCNCC saturates at a nonzero value depending on δ .

From our simulation results for the considered scenario, we further remark that we observe the parameter estimates approaching the true parameters in the noise-free case, which suggests that in this case, our

modified BCD algorithm converges to the global minimum of problem (15).

5.2. Real data

For experimental validation, we use an 8×8 URA with custom electronics based on a Xilinx Zynq 7010 FPGA [54]. The URA features PUTs of type MA40S4S manufactured by Murata (Nagaokakyo, Kyoto Prefecture, Japan). The MA40S4S operate at $f_0 = 40$ kHz and have an output power level of more than 120 dB at 0.3 m, enabling imaging ranges of several meters. These transducers are widely available to both academic and commercial customers, however, their bulky dimensions prevent a classic $\lambda/2$ -spacing between neighboring array elements. An individually designed waveguide has been proposed to overcome this limitation and is part of the considered URA [22].

All URA elements can operate in both transmit and receive mode, with fast switching for simultaneous pulse transmission and reception. However, to avoid ring-out effects, we use each transceiver exclusively as a transmitter or receiver. Specifically, the $N = 4$ corner transducers sequentially transmit sinusoidal pulses of duration $T_{\text{burst}} = 1$ ms each. This configuration minimizes measurement time, limited by the number of pulses per calibration position.

For both calibration and imaging, we fire $T = 10$ pulses from one transmitter before switching to the next, repeating this until all $N = 4$ transmitters have emitted in total $NT = 40$ bursts. The remaining $M = 60$ sensor elements in the URA operate in receive mode only. For each snapshot $t = 1, \dots, T$, echoes are recorded at a sampling frequency $f_s = 195$ kHz and stored for $L = 24$ sample frequencies. Unambiguous range detection within the bounds of the anechoic chamber is ensured by setting the pulse repetition rate to $\Delta T_{\text{burst}} = 150$ ms, assuming a wave propagation velocity of $c = 343$ ms $^{-1}$.

We select $P = 1909$ calibration points distributed on a spherical shell at a constant range of $r = 2$ m, covering a FOV of $\pm 60^\circ$ in both azimuth and elevation. Near broadside, the FOV is sampled more densely due to a higher sensitivity of the steering vectors \mathbf{a}_p at lower electrical angles $\arg(\mathbf{a}_p)$. The exact coordinates of each point p are derived from the rotational axes of the measurement system, which efficiently move the array relative to the calibration target along a meander-shaped path [76].

The reconstruction performance of our algorithm for the US array measurements described above is shown in Fig. 4. In Fig. 4(a), the relative pointwise reconstruction error

$$\zeta_{\text{rel}}(p) = \left(\|\mathbf{y}_p\|_F \right)^{-1} \|\mathbf{y}_p - \hat{\mathbf{y}}_p\|_F \quad (50)$$

is displayed for various azimuth and elevation angles at the set range of $r = 2$ m. The relative reconstruction error represents the model mismatch for any calibration position $p = 1, \dots, P$ between the calibration measurement \mathbf{y}_p and the reconstructed model $\hat{\mathbf{y}}_p$ according to (3) using the parameter estimates learned with our modified BCD algorithm. We observe that our proposed tensor model in (3) accurately models measured data for different target positions within the FOV, despite the narrow 3 dB mainlobe width of 12° [54]. The relative pointwise reconstruction error according to (50) is 20% near broadside and increases up to 50% towards the edge of the FOV. The reconstruction errors may be due to measurement noise, model errors resulting from the violation of the single-point-source assumption, and reverberation. By construction, the BCD method always provides a decrease of the objective function in every variable update. The convergence behavior of our proposed modified BCD method is shown by examining the difference between the normalized cost function $f_{\text{rel}}^{(i)}$ according to (49) at each iteration i against $f_{\text{rel}}^{(i-1)}$ of the previous iteration (Fig. 4(b)).

Finally, projections of scatter plots in Cartesian and spherical space are given as a proof-of-concept for the imaging capabilities of the proposed model and methods. As a test scenario, we arrange multiple tetrahedral corner reflectors of the same kind as used for calibration on

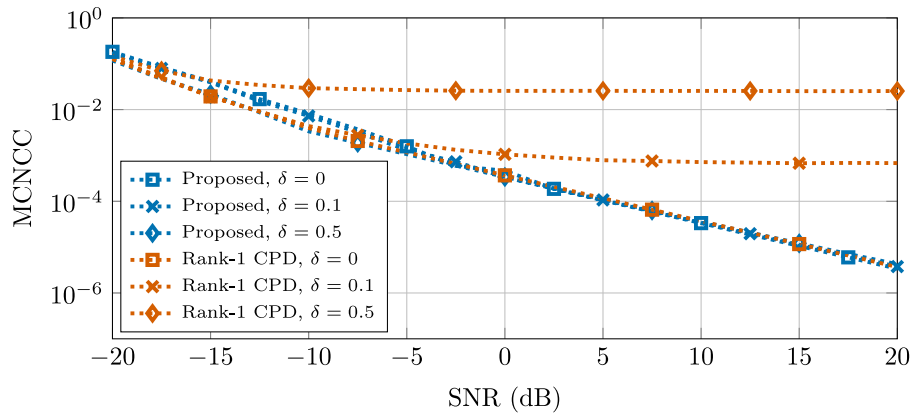
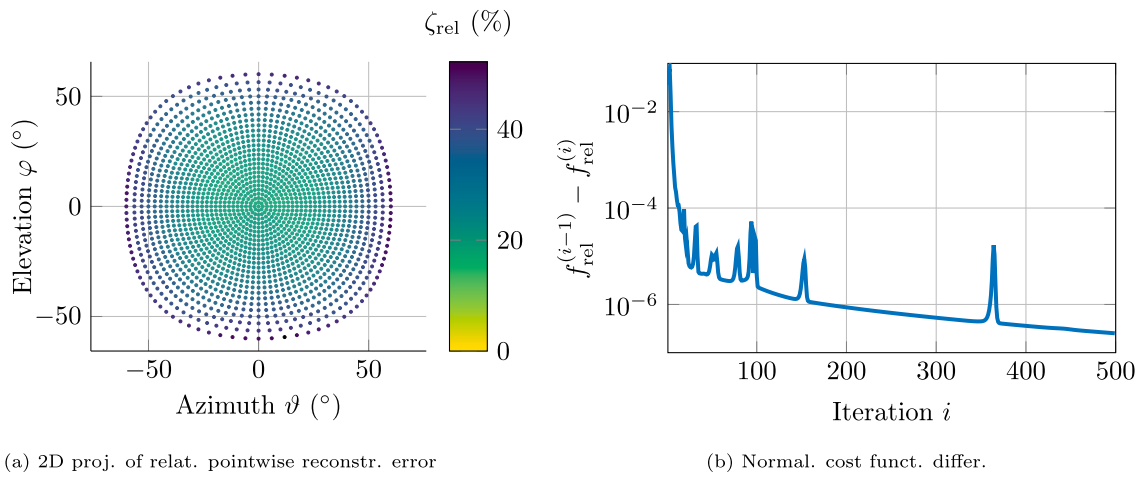


Fig. 3. Comparison between our proposed decomposition method and a rank-1 CPD approximation, respectively, using the mean complementary normalized cross-correlation (MCNCC) (48) of the vectorized range-angle response estimates \hat{q}_p and their respective true values q_p according to (42). Unlike the rank-1 CPD, our proposed method is independent of the frequency response variation δ .



(a) 2D proj. of relat. pointwise reconstr. error

(b) Normal. cost funcn. differ.

Fig. 4. Relative pointwise reconstruction error (50) and normalized cost function difference (49) of the calibration technique proposed in Section 3 in a constant range of $r = 2$ m. For $P = 1909$ calibration points defined by their azimuth ϑ and elevation φ w.r.t. the alignment of the array elements, the reconstruction error $\zeta_{\text{rel}(p)}$ is computed after 500 iterations (a). To show the convergence behavior, the difference $f_{\text{rel}}^{(i-1)} - f_{\text{rel}}^{(i)}$ between consecutive normalized cost function values is evaluated (b).

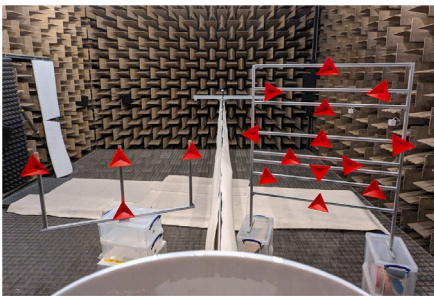


Fig. 5. Imaging setup with multiple targets (red triangles) viewed from above and behind the rigid baffle.

two skew planes perpendicular to the x - z plane (Fig. 5). A dictionary of $P = R \cdot P_{\text{measured}} = 15 \cdot 1909 = 28,635$ range-angle response vectors $\{q_p\}_{p=1}^P$ is learned from $P_{\text{measured}} = 1909$ measured calibration positions with varying angles at the constant range $r = 2$ m and $R = 15$ different scanning ranges r' including the original calibration range. The scanning ranges are chosen as $r' = r + 0.2 \cdot k \cdot \Delta r$, $k = -7, \dots, 7$, where $\Delta r = 0.5 \cdot c \cdot T_{\text{burst}} \approx 17$ cm equals half the range resolution given by the Rayleigh bandwidth [77]. For imaging, we apply the OMP algorithm introduced in Section 4 with $I_{\text{OMP}} = 100$ iterations.

In each iteration, we select one range-angle response vector $q_{\hat{p}}$ from the dictionary according to Step 1 in (45). The corresponding position estimate \hat{p} is assigned the weighted norm square $T^{-2} \|\hat{h}_{\hat{p}}\|_2^2$ according to Step 2 in (47). A threshold is then applied to exclude position estimates \hat{p} with a weighted power estimate $T^{-2} \|\hat{h}_{\hat{p}}\|_2^2$ more than 10 dB below the peak estimate. The remaining target estimates are color-coded according to their weighted power estimate.

A 2D image of the reconstructed model projected onto the x - z plane is displayed in Fig. 6(a) while Fig. 6(b) shows an angular projection using azimuth and elevation. The latter is obtained by transforming Cartesian coordinates into spherical ones and collapsing the range dimension of the resulting tensor. A positive azimuth angle ϑ is measured from the z -axis to the x -axis whereas a positive elevation angle φ is measured from the z -axis to the y -axis. Signal gains associated to targets appearing under the same direction, i.e. same azimuth and elevation but different scanning ranges, are added up. For comparison, we provide the 2D projection based on an analytic dictionary that requires exact array geometry knowledge and is used without and with the broadside compensation from Section 3.9 (c.f. Figs. 6(c) and (d), respectively).

Our main observations from Fig. 6 are threefold:

- (1) In our proof-of-concept experiment with real data, Fig. 6(b) shows that we achieve a good imaging performance because the proposed dictionary of measured array responses, i.e. without

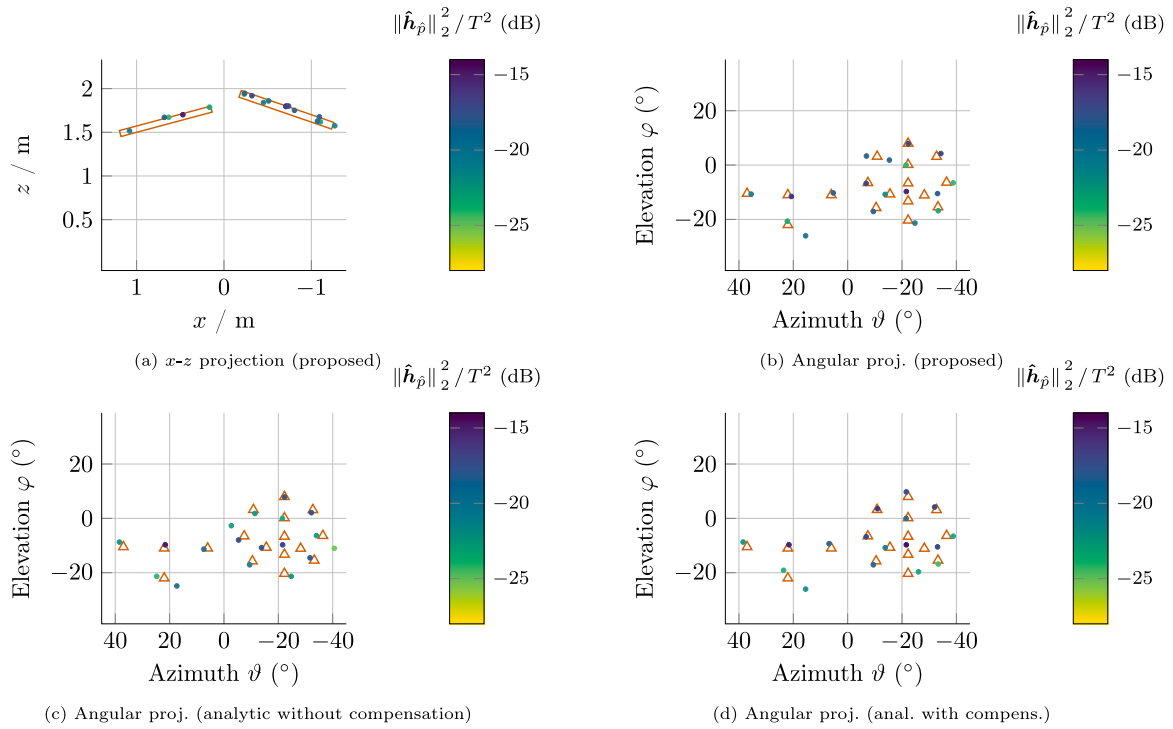


Fig. 6. From measurements with multiple reflectors (red), scatter plots projected onto the x - z plane (a) and the azimuth-elevation-plane (b), respectively, are computed using the dictionary of our proposed calibration method. For comparison, the angular projections using an analytic dictionary without (c) and with (d) broadside compensation are also provided.

explicit knowledge of the array geometry, is capable of resolving the multi-target scenario.

- (2) Fig. 6(a) shows that the principal target location estimates \hat{p} corresponding to larger signal gain estimates \hat{h}_p are distributed along two planes perpendicular to the x - z -plane according to the ground truth setup indicated by the red boxes. This proves the correctness of our assumed linear phase response model in (35): target ranges can be estimated even if they have not been learned during calibration.
- (3) Without and with broadside compensation (c.f. Figs. 6(c) and (d), respectively), the analytic model, which requires precise knowledge of the array geometry, yields similar imaging performance as obtained with the array responses learned from calibration measurements.

6. Conclusions and outlook

In this article, we propose a novel tensor model to describe the measurement data of an air-coupled ultrasonic MIMO sensor array for 3D imaging. A reference-based calibration scheme is suggested in which the tensor model parameters are jointly estimated from all calibration measurements using a modified BCD method with proven convergence. The modification exploits scaling invariances between the block variables to convert the originally nonconvex subproblems into equivalent subproblems that admit closed-form solutions. Numerical experiments carried out with synthetic data as well as real measurements recorded with an air-coupled ultrasonic array confirm both, the validity of the model as well as the functionality of the calibration procedure. Additionally, an imaging example with real data verifies that dictionaries with the commonly used, analytically modeled steering and phase response vectors as well as the angular-range response vectors obtained with our calibration procedure are feasible for 3D imaging with air-coupled ultrasonic sensor arrays. It is assumed that in air-coupled US as well as other array processing applications such as radar or sonar, array elements with magnitude responses more distinct than those of

our prototype array will benefit from our proposed model as suggested by our simulations.

In the future, we will investigate if more structure enforced onto the tensor signal model and therefore the optimization problem itself, e.g. by exploiting a parametric range model during calibration, will improve the calibration results and imaging performance. Future work also addresses performance bounds of the proposed tensor model and research towards non-reference-based, i.e. blind, calibration methods that perform joint calibration and imaging without the overhead associated with calibration measurements.

CRediT authorship contribution statement

Raphael Müller: Writing – review & editing, Writing – original draft, Visualization, Methodology, Investigation, Formal analysis, Conceptualization. **Gianni Allevato:** Writing – review & editing, Resources. **Matthias Rutsch:** Writing – review & editing, Resources. **Christoph Haugwitz:** Writing – review & editing, Resources. **Tianyi Liu:** Formal analysis. **Mario Kupnik:** Writing – review & editing, Resources. **Marius Pesavento:** Writing – review & editing, Validation, Supervision, Conceptualization.

Acknowledgments

This work has received funding from the German Federal Ministry of Education and Research (BMBF) within the project “Open6GHub” under grant number 16KISK014.

Data availability

Data will be made available on request.

References

- [1] J. Huang, X. Yang, Fast reduction of speckle noise in real ultrasound images, *Signal Process.* 93 (4) (2013) 684–694, <http://dx.doi.org/10.1016/j.sigpro.2012.09.005>.
- [2] C. Yu, C. Zhang, L. Xie, An envelope signal based deconvolution algorithm for ultrasound imaging, *Signal Process.* 92 (3) (2012) 793–800, <http://dx.doi.org/10.1016/j.sigpro.2011.09.024>.
- [3] M.K. Kiyimik, I. Güler, O. Hasekioglu, M. Karaman, Ultrasound imaging based on multiple beamforming with coded excitation, *Signal Process.* 58 (1) (1997) 107–113, [http://dx.doi.org/10.1016/S0165-1684\(97\)00016-9](http://dx.doi.org/10.1016/S0165-1684(97)00016-9).
- [4] S. Harput, A. Bozkurt, Ultrasonic phased array device for acoustic imaging in air, *IEEE Sens. J.* 8 (11) (2008) 1755–1762, <http://dx.doi.org/10.1109/JSEN.2008.2004574>.
- [5] J.F. Synnevag, A. Austeng, S. Holm, Adaptive beamforming applied to medical ultrasound imaging, *IEEE Open J. Ultrason. Ferroelectr. Freq. Contr.* 54 (8) (2007) 1606–1613, <http://dx.doi.org/10.1109/TUFFC.2007.431>.
- [6] J.A. Jensen, S.I. Nikolov, K.L. Gammelmark, M.H. Pedersen, Synthetic aperture ultrasound imaging, *Ultrason.* 44 (2006) e5–e15, <http://dx.doi.org/10.1016/j.ultras.2006.07.017>.
- [7] T.G. Leighton, What is ultrasound? *Prog. Biophys. Mol. Biol.* 93 (1) (2007) 3–83, <http://dx.doi.org/10.1016/j.pbiomolbio.2006.07.026>.
- [8] A.S. Mohammed, A. Amamou, F.K. Ayevide, S. Kelouani, K. Agbowski, N. Zioui, The perception system of intelligent ground vehicles in all weather conditions: A systematic literature review, *Sensors* 20 (22) (2020) 6532, <http://dx.doi.org/10.3390/s20226532>.
- [9] S.M. Patole, M. Torlak, D. Wang, M. Ali, Automotive radars: A review of signal processing techniques, *IEEE Signal Process. Mag.* 34 (2) (2017) 22–35, <http://dx.doi.org/10.1109/MSP.2016.2628914>.
- [10] Z. Fang, F. Gao, H. Jin, S. Liu, W. Wang, R. Zhang, Z. Zheng, X. Xiao, K. Tang, L. Lou, K.-T. Tang, J. Chen, Y. Zheng, A review of emerging electromagnetic-acoustic sensing techniques for healthcare monitoring, *IEEE Trans. Biomed. Circuits Syst.* 16 (6) (2022) 1075–1094, <http://dx.doi.org/10.1109/TBCAS.2022.3226290>.
- [11] D.E. Chimenti, Review of air-coupled ultrasonic materials characterization, *Ultrason.* 54 (7) (2014) 1804–1816, <http://dx.doi.org/10.1016/j.ultras.2014.02.006>.
- [12] M. Haller, B. Khuri-Yakub, 1-3 composites for ultrasonic air transducers, in: *IEEE 1992 Ultrason. Symp., Vol. 2, 1992*, pp. 937–939, <http://dx.doi.org/10.1109/ULTSYM.1992.275822>.
- [13] F. Lionetto, A. Tarzia, A. Maffezzoli, Air-coupled ultrasound: A novel technique for monitoring the curing of thermosetting matrices, *IEEE Trans. Ultrason. Ferroelectr. Freq. Control* 54 (7) (2007) 1437–1444, <http://dx.doi.org/10.1109/TUFFC.2007.404>.
- [14] H.E. Bass, L.C. Sutherland, A.J. Zuckerwar, Atmospheric absorption of sound: Update, *J. Acoust. Soc. Am.* 88 (4) (1990) 2019–2021, <http://dx.doi.org/10.1121/1.400176>.
- [15] M. Strakowski, B. Kosmowski, R. Kowalik, P. Wierzba, An ultrasonic obstacle detector based on phase beamforming principles, *IEEE Sens. J.* 6 (1) (2006) 179–186, <http://dx.doi.org/10.1109/JSEN.2005.856129>.
- [16] T. Dahl, J.L. Ealo, H.J. Bang, S. Holm, P. Khuri-Yakub, Applications of airborne ultrasound in human-computer interaction, *Ultrason.* 54 (7) (2014) 1912–1921, <http://dx.doi.org/10.1016/j.ultras.2014.04.008>.
- [17] S. Suzuki, S. Inoue, M. Fujiwara, Y. Makino, H. Shinoda, AUTD3: Scalable airborne ultrasound tactile display, *IEEE Trans. Haptics* 14 (4) (2021) 740–749, <http://dx.doi.org/10.1109/TOH.2021.3069976>.
- [18] M. Legg, S. Bradley, Ultrasonic arrays for remote sensing of pasture biomass, *Remote Sens.* 12 (1) (2020) 111, <http://dx.doi.org/10.3390/rs12010111>.
- [19] A.S. Rekhii, B.T. Khuri-Yakub, A. Arbabian, Wireless power transfer to millimeter-sized nodes using airborne ultrasound, *IEEE Trans. Ultrason. Ferroelectr. Freq. Control* 64 (10) (2017) 1526–1541, <http://dx.doi.org/10.1109/TUFFC.2017.2737620>.
- [20] A. Marzo, S.A. Seah, B.W. Drinkwater, D.R. Sahoo, B. Long, S. Subramanian, Holographic acoustic elements for manipulation of levitated objects, *Nature Commun.* 6 (1) (2015) 8661, <http://dx.doi.org/10.1038/ncomms9661>.
- [21] J. Gelly, F. Lanteri, Comparison of piezoelectric (thickness mode) and MEMS transducers, in: *IEEE Symp. Ultrason., Vol. 2, 2003*, pp. 1965–1974, <http://dx.doi.org/10.1109/ULTSYM.2003.1293302>, Vol.2.
- [22] A. Jäger, D. Großkurth, M. Rutsch, A. Unger, R. Golinske, H. Wang, S. Dixon, K. Hofmann, M. Kupnik, Air-coupled 40-KHz ultrasonic 2D-phased array based on a 3D-printed waveguide structure, in: *IEEE Int. Ultrason. Symp., IUS, 2017*, pp. 1–4, <http://dx.doi.org/10.1109/ULTSYM.2017.8091892>.
- [23] M. Viberg, M. Lanne, A. Lundgren, Calibration in array processing, in: T.E. Tuncer, B. Friedlander (Eds.), *Classical and Modern Direction-of-Arrival Estimation*, Elsevier Inc., Burlington, 2009, pp. 93–124, <http://dx.doi.org/10.1016/B978-0-12-374524-8.00003-9>.
- [24] G. Wu, M. Zhang, F. Guo, Self-calibration direct position determination using a single moving array with sensor gain and phase errors, *Signal Process.* 173 (2020) 107587, <http://dx.doi.org/10.1016/j.sigpro.2020.107587>.
- [25] B.C. Ng, C.M.S. See, Sensor-array calibration using a maximum-likelihood approach, *IEEE Trans. Antennas and Propagation* 44 (6) (1996) 827–835, <http://dx.doi.org/10.1109/8.509886>.
- [26] M. Viberg, A.L. Swindlehurst, A Bayesian approach to auto-calibration for parametric array signal processing, *IEEE Trans. Signal Process.* 42 (12) (1994) 3495–3507, <http://dx.doi.org/10.1109/78.340783>.
- [27] A.J. Weiss, B. Friedlander, Array shape calibration using sources in unknown locations—a maximum likelihood approach, *IEEE Trans. Acoust. Speech Signal Process.* 37 (12) (1989) 1958–1966, <http://dx.doi.org/10.1109/29.45542>.
- [28] K. Han, P. Yang, A. Nehorai, Calibrating nested sensor arrays with model errors, *IEEE Trans. Antennas and Propagation* 63 (11) (2015) 4739–4748, <http://dx.doi.org/10.1109/TAP.2015.2477411>.
- [29] A. Liu, G. Liao, C. Zeng, Z. Yang, Q. Xu, An eigenstructure method for estimating DOA and sensor gain-phase errors, *IEEE Trans. Signal Process.* 59 (12) (2011) 5944–5956, <http://dx.doi.org/10.1109/TSP.2011.2165064>.
- [30] Z. Liu, Z. Huang, F. Wang, Y. Zhou, DOA estimation with uniform linear arrays in the presence of mutual coupling via blind calibration, *Signal Process.* 89 (7) (2009) 1446–1456, <http://dx.doi.org/10.1016/j.sigpro.2009.01.017>.
- [31] Y. Liu, B. Jiu, H. Liu, Clutter-based gain and phase calibration for monostatic MIMO radar with partly calibrated array, *Signal Process.* 158 (2019) 219–226, <http://dx.doi.org/10.1016/j.sigpro.2019.01.011>.
- [32] B. Liao, S.C. Chan, Direction finding with partly calibrated uniform linear arrays, *IEEE Trans. Antennas and Propagation* 60 (2) (2012) 922–929, <http://dx.doi.org/10.1109/TAP.2011.2173144>.
- [33] P. Parvazi, M. Pesavento, A.B. Gershman, Direction-of-arrival estimation and array calibration for partly-calibrated arrays, in: *2011 IEEE Int. Conf. Acoust. Speech Signal Process., ICASSP, 2011*, pp. 2552–2555, <http://dx.doi.org/10.1109/ICASSP.2011.5947005>.
- [34] H. Wan, B. Liao, Fourth-order direction finding in antenna arrays with partial channel gain/phase calibration, *Signal Process.* 169 (2020) 107380, <http://dx.doi.org/10.1016/j.sigpro.2019.107380>.
- [35] H. Huang, Q. Liu, H.C. So, A.M. Zoubir, Low-rank and row-sparse decomposition for joint DOA estimation and distorted sensor detection, *IEEE Trans. Aerosp. Electron. Syst.* 59 (4) (2023) 4763–4773, <http://dx.doi.org/10.1109/TAES.2023.3241886>.
- [36] J. Geiss, E. Sippel, M. Hehn, M. Vossiek, Antenna array calibration using a sparse scene, *IEEE Open J. Antennas Propag.* 2 (2021) 349–361, <http://dx.doi.org/10.1109/OJAP.2021.3061935>.
- [37] M.J. Taghizadeh, R. Parhizkar, P.N. Garner, H. Bourlard, A. Asaei, Ad hoc microphone array calibration: Euclidean distance matrix completion algorithm and theoretical guarantees, *Signal Process.* 107 (2015) 123–140, <http://dx.doi.org/10.1016/j.sigpro.2014.07.016>.
- [38] K.N. Ramamohan, S.P. Chepuri, D.F. Comesaña, G. Leus, Self-calibration of acoustic scalar and vector sensor arrays, *IEEE Trans. Signal Process.* 71 (2023) 61–75, <http://dx.doi.org/10.1109/TSP.2022.3214383>.
- [39] V. Ollier, M.N.E. Korso, R. Boyer, P. Larzabal, M. Pesavento, Robust calibration of radio interferometers in non-Gaussian environment, *IEEE Trans. Signal Process.* 65 (21) (2017) 5649–5660, <http://dx.doi.org/10.1109/TSP.2017.2733496>.
- [40] J. Pierre, M. Kaveh, Experimental performance of calibration and direction-finding algorithms, in: *1991 Int. Conf. Acoust. Speech Signal Process., ICASSP, Vol. 2, 1991*, pp. 1365–1368, <http://dx.doi.org/10.1109/ICASSP.1991.150676>.
- [41] A. Paulraj, T. Kailath, Direction of arrival estimation by eigenstructure methods with unknown sensor gain and phase, in: *1985 IEEE Int. Conf. Acoust. Speech Signal Process., ICASSP, Vol. 10, 1985*, pp. 640–643, <http://dx.doi.org/10.1109/ICASSP.1985.1168341>.
- [42] J.A. Nanzer, S.R. Mghabghab, S.M. Ellison, A. Schlegel, Distributed phased arrays: Challenges and recent advances, *IEEE Trans. Microw. Theory Tech.* 69 (11) (2021) 4893–4907, <http://dx.doi.org/10.1109/TMTT.2021.3092401>.
- [43] P. Heidenreich, A.M. Zoubir, M. Rubsamen, Joint 2-D DOA estimation and phase calibration for uniform rectangular arrays, *IEEE Trans. Signal Process.* 60 (9) (2012) 4683–4693, <http://dx.doi.org/10.1109/TSP.2012.2203125>.
- [44] S.J. Wijnholds, A.-J. van der Veen, Multisource self-calibration for sensor arrays, *IEEE Trans. Signal Process.* 57 (9) (2009) 3512–3522, <http://dx.doi.org/10.1109/TSP.2009.2022894>.
- [45] I. Tošić, P. Frossard, Dictionary learning, *IEEE Signal Process. Mag.* 28 (2) (2011) 27–38, <http://dx.doi.org/10.1109/MSP.2010.939537>.
- [46] Y. Guo, X. Wang, L. Wan, M. Huang, C. Shen, K. Zhang, Y. Yang, Tensor-based angle and array gain-phase error estimation scheme in bistatic MIMO radar, *IEEE Access* 7 (2019) 47972–47981, <http://dx.doi.org/10.1109/ACCESS.2019.2909760>.
- [47] Y. Sun, W.-Q. Wang, C. Jiang, Space-time-range clutter suppression via tensor-based STAP for airborne FDA-MIMO radar, *Signal Process.* 214 (2024) 109235, <http://dx.doi.org/10.1016/j.sigpro.2023.109235>.
- [48] J. Chen, Y. Tang, X. Zhu, J. Li, Angle estimation based on Vandermonde constrained CP tensor decomposition for bistatic MIMO radar under spatially colored noise, *Signal Process.* 220 (2024) 109429, <http://dx.doi.org/10.1016/j.sigpro.2024.109429>.
- [49] R. Müller, D. Schenck, G. Allevato, M. Rutsch, J. Hinrichs, M. Kupnik, M. Pesavento, Dictionary-based learning for 3D-imaging with air-coupled ultrasonic phased arrays, in: *IEEE Int. Ultrason. Symp., IUS, 2020*, pp. 1–4, <http://dx.doi.org/10.1109/IUS46767.2020.9251726>.

- [50] G. Kushe, Y. Yang, C. Steffens, M. Pesavento, A parallel sparse regularization method for structured multilinear low-rank tensor decomposition, in: 27th Eur. Signal Process. Conf., EUSIPCO, 2019, pp. 1–5, <http://dx.doi.org/10.23919/EUSIPCO.2019.8902569>.
- [51] J. Liu, J. Li, Robust detection in MIMO radar with steering vector mismatches, *IEEE Trans. Signal Process.* 67 (20) (2019) 5270–5280, <http://dx.doi.org/10.1109/TSP.2019.2939078>.
- [52] M. Rutsch, A. Unger, G. Allevalo, J. Hinrichs, A. Jäger, T. Kaindl, M. Kupnik, Waveguide for air-coupled ultrasonic phased-arrays with propagation time compensation and plug-in assembly, *J. Acoust. Soc. Am.* 150 (5) (2021) 3228–3237, <http://dx.doi.org/10.1121/10.0006969>.
- [53] M. Viberg, Introduction to array processing, in: A.M. Zoubir, M. Viberg, R. Chellappa, S. Theodoridis (Eds.), *Array and Statistical Signal Processing*, in: Academic Press Library in Signal Processing, vol. 3, Elsevier Ltd., Kidlington, UK, 2014, pp. 463–502, <http://dx.doi.org/10.1016/B978-0-12-411597-2.00011-4>.
- [54] G. Allevalo, J. Hinrichs, M. Rutsch, J.P. Adler, A. Jäger, M. Pesavento, M. Kupnik, Real-time 3-D imaging using an air-coupled ultrasonic phased-array, *IEEE Trans. Ultrason. Ferroelectr. Freq. Control* 68 (3) (2021) 796–806, <http://dx.doi.org/10.1109/TUFFC.2020.3005292>.
- [55] W.L. Melvin, Space-time adaptive processing for radar, in: N.D. Sidiropoulos, F. Gini, R. Chellappa, S. Theodoridis (Eds.), *Communications and Radar Signal Processing*, in: Academic Press Library in Signal Processing, vol. 2, Elsevier Ltd., Kidlington, UK, 2014, pp. 595–665, <http://dx.doi.org/10.1016/B978-0-12-396500-4.00012-0>.
- [56] G. Allevalo, *Ultrasonic Phased Arrays for 3D Sonar Imaging in Air* (Ph.D. thesis), Technische Universität Darmstadt, Darmstadt, Germany, 2023, <http://dx.doi.org/10.26083/tuprints-00024425>.
- [57] J.D. Carroll, J.-J. Chang, Analysis of individual differences in multidimensional scaling via an n -way generalization of “Eckart-Young” decomposition, *Psychometrika* 35 (3) (1970) 283–319, <http://dx.doi.org/10.1007/BF02310791>.
- [58] R.A. Harshman, *Foundations of the PARAFAC Procedure: Models and Conditions for an “Explanatory” Multi-Modal Factor Analysis*, *UCLA Working Papers in Phonetics* 16, Ann Arbor, Michigan, 1970, pp. 1–84.
- [59] L. De Lathauwer, Decompositions of a higher-order tensor in block terms—Part II: Definitions and uniqueness, *SIAM J. Matrix Anal. Appl.* 30 (3) (2008) 1033–1066, <http://dx.doi.org/10.1137/070690729>.
- [60] A. Cichocki, D. Mandic, L. De Lathauwer, G. Zhou, Q. Zhao, C. Caiifa, H.A. PHAN, Tensor decompositions for signal processing applications: From two-way to multiway component analysis, *IEEE Signal Process. Mag.* 32 (2) (2015) 145–163, <http://dx.doi.org/10.1109/MSP.2013.2297439>.
- [61] T.G. Kolda, B.W. Bader, Tensor decompositions and applications, *SIAM Rev.* 51 (3) (2009) 455–500, <http://dx.doi.org/10.1137/07070111X>.
- [62] H.A.L. Kiers, Towards a standardized notation and terminology in multiway analysis, *J. Chemom.* 14 (3) (2000) 105–122, [http://dx.doi.org/10.1002/1099-128X\(200005/06\)14:3<105::AID-CEM582>3.0.CO;2-I](http://dx.doi.org/10.1002/1099-128X(200005/06)14:3<105::AID-CEM582>3.0.CO;2-I).
- [63] N.D. Sidiropoulos, L. De Lathauwer, X. Fu, K. Huang, E.E. Papalexakis, C. Faloutsos, Tensor decomposition for signal processing and machine learning, *IEEE Trans. Signal Process.* 65 (13) (2017) 3551–3582, <http://dx.doi.org/10.1109/TSP.2017.2690524>.
- [64] A. Paulraj, B. Ottersten, R. Roy, A. Swindlehurst, G. Xu, T. Kailath, Subspace methods for directions-of-arrival estimation, in: N.K. Bose, C.R. Rao (Eds.), *Handbook of Statistics*, Vol. 10, Elsevier Science Publishers B.V., 1993, pp. 693–739.
- [65] Y. Yang, M. Pesavento, Z.-Q. Luo, B. Ottersten, Inexact block coordinate descent algorithms for nonsmooth nonconvex optimization, *IEEE Trans. Signal Process.* 68 (2020) 947–961, <http://dx.doi.org/10.1109/TSP.2019.2959240>.
- [66] D.P. Bertsekas, *Nonlinear Programming*, third ed., Athena Scientific, Belmont, 2016.
- [67] M.A. Richards, J.A. Scheer, W.A. Holm (Eds.), *Principles of Modern Radar: Basic Principles*, Vol. 1, SciTech Publishing, Raleigh (NC), 2010.
- [68] R. Roy, T. Kailath, ESPRIT-estimation of signal parameters via rotational invariance techniques, *IEEE Trans. Acoust. Speech Signal Process.* 37 (7) (1989) 984–995, <http://dx.doi.org/10.1109/29.32276>.
- [69] H.M. Aumann, F.G. Willwerth, *Phased-array calibration by adaptive nulling*, *Tech. Rep. 915*, Lincoln Laboratory/Massachusetts Institute of Technology, Lexington/Massachusetts, 1991.
- [70] R. Kerstens, D. Laurijssen, J. Steckel, eRTIS: A fully embedded real time 3D imaging sonar sensor for robotic applications, in: *Int. Conf. Robotics Autom., ICRA*, 2019, pp. 1438–1443, <http://dx.doi.org/10.1109/ICRA.2019.8794419>.
- [71] R.O. Schmidt, Multiple emitter location and signal parameter estimation, *IEEE Trans. Antennas and Propagation* 34 (3) (1986) 276–280, <http://dx.doi.org/10.1109/TAP.1986.1143830>.
- [72] Z. Zhang, Y. Xu, J. Yang, X. Li, D. Zhang, A survey of sparse representation: Algorithms and applications, *IEEE Access* 3 (2015) 490–530, <http://dx.doi.org/10.1109/ACCESS.2015.2430359>.
- [73] M. Pesavento, M. Trinh-Hoang, M. Viberg, Three more decades in array signal processing research: An optimization and structure exploitation perspective, *IEEE Signal Process. Mag.* 40 (4) (2023) 92–106, <http://dx.doi.org/10.1109/MSP.2023.3255558>.
- [74] Y. Pati, R. Rezaifar, P. Krishnaprasad, Orthogonal matching pursuit: Recursive function approximation with applications to wavelet decomposition, in: *Proc. 27th Asilomar Conf. Signals Syst. Comput.*, Vol. 1, 1993, pp. 40–44, <http://dx.doi.org/10.1109/ACSSC.1993.342465>.
- [75] D.L. Donoho, X. Huo, Uncertainty principles and ideal atomic decomposition, *IEEE Trans. Inform. Theory* 47 (7) (Nov./2001) 2845–2862, <http://dx.doi.org/10.1109/18.959265>.
- [76] M. Rutsch, *Duct Acoustics for Air-Coupled Ultrasonic Phased Arrays* (Ph.D. thesis), Technische Universität Darmstadt, Darmstadt, Germany, 2023.
- [77] M.A. Richards, *Fundamentals of Radar Signal Processing*, third ed., McGraw Hill, New York, 2022.